Evaluating the performance of PATMOS-x in global and regional analyses of clouds as they relate to Earth's planetary albedo

Erica L. Bortfeldt

A thesis submitted in partial fulfillment of the requirements for the degree of

Master of Science
Atmospheric and Oceanic Sciences

at the

UNIVERSITY OF WISCONSIN-MADISON

(August, 2025)

Acknowledgements

The research presented in this thesis has been brought forth by a collaborative effort among infinitely valuable mentors, peers, colleagues, friends, and family, all of whom represent the determination to persevere in the pursuit of truth and ethical practice at a time when such principles have become all too rare. As it stands, one cannot dissolve the intimate entanglement of climate science with political discordance; it is, perhaps, one of the single most contentious subjects afflicting modern society on a global scale. In such a sundered environment, where the merit of science is confronted with significant animosity and increasingly weighed against the tempting fallacies of disinformation, I have had the great privilege of watching my fellow meteorologists, climatologists, and oceanographers rise unflinchingly to the challenge of fighting for the future of our field in the face of silence and suppression. During my tenure in the Department of Atmospheric and Oceanic Sciences at UW-Madison, I encountered no soul braver than the students I shared countless classroom hours with – intrepid in their pursuit of knowledge to serve the vision of a just future, the professors whose boundless wisdom and guidance I sought often in times of frustration and uncertainty, and the administrators who championed every student's right to study our endangered discipline. It is with the fullest heart that I extend my sincere acknowledgements to these extraordinary scholars and advocates.

I would especially like to profess my eternal gratitude to my advisors, Mike Foster, Tristan L'Ecuyer, and Mayra Oyola-Merced, each of whom oversaw my development as a young scientist with great care, compassion, and enthusiasm. As well, I would like to thank Coda Phillips for his patience and investment in my success, despite my stubborn resistance to change in my approach to things, Hannah Zanowski, who went to immense lengths to keep me grounded in my own strength and will to persist, Angela Rowe, who helped me fall in love with research and taught me to always pursue my interests with unshakeable fervor, and Kaitlyn Heinlein, who never stopped supporting me and always expressed keen interest in my endeavors, even after I was no longer under her advisement. Lastly, I want to thank my mother, Sue, and father, Paul, who ensured I had the opportunities and resources to chase my goals freely, my brother, Kyle, whose fascination and passion for the sciences inspired my own, and my sister, Shannon, whose affinity for the arts lent itself to my development of unique perspectives and creativity in problem-solving. All of these people made me the scientist I am today, and for that, I am tremendously thankful.

Abstract

In 2023, the Clouds and the Earth's Radiant Energy System - Energy Balanced and Filled (CERES-EBAF) dataset revealed a record low planetary albedo. Due to the dominant role of clouds in Earth's albedo, we hypothesize that the negative anomaly identified in 2023 is most likely a consequence of a similar anomaly in cloud fraction and, subsequently, effective reflectance. Since the CERES-EBAF dataset cannot be used for in-depth analyses of cloud behavior, as it is limited by a narrow selection of cloud property variables, the visible reflectance parameter featured in the Pathfinder Atmospheres-Extended (PATMOS-x) v6.0 dataset – a 1980-present global satellite record with a primary focus on cloud properties – is proposed as a supplement for investigating the relative contribution of clouds to the 2023 albedo anomaly. However, because PATMOS-x incorporates data from Advanced Very-High Resolution Radiometers (AVHRRs) flown on sixteen separate satellite platforms, each of which has its own set of calibration coefficients, local overpass times, and degrees of orbital drift, synthesizing a stable, long-term record of global visible reflectance is not possible without radiometric normalization and frequent updates to the intercalibration.

Presented here is a novel approach to validating the most recent PATMOS-x v6.0 visible reflectance calibration, wherein tropical deep convective clouds (DCCs) are used as climatologically predictable targets to evaluate reflective stability over time and develop a solar zenith angle-dependent normalization method for handling the impacts of orbital drift and local overpass time discrepancies. While a robust validation of the record's visible intercalibration is obtained in a strictly-controlled context, the normalization methodology applied to DCCs in the Tropics does not necessarily handle orbital drift and local overpass time discrepancies to an adequate extent when it is applied (a) to a broader array of cloud types, (b) on a global scale, and

(c) for the entire duration of the record. Alternatively, in a case study of the Central Indian Ocean, the PATMOS-x record demonstrates a reasonable capacity to produce accurate ocean-based regional analyses of cloud effective reflectance between 2000 and 2023. Impacts owed to orbital drift and local overpass differences are better-resolved by the solar zenith angle normalization when analysis is centered over a relatively localized oceanic region; it is, thus, more feasible to draw conclusive results of cloud fraction and, consequently, effective reflectance under this circumstance. It is ultimately determined that, over the Central Indian Ocean, the local planetary albedo anomaly in 2023 is the result of a pronounced negative anomaly in upper-level cloud fraction, primarily contributed to by clouds in the 3.6-23 range of optical depth and ~30-45% range of mean reflectance.

Table of Contents

List of Figures

Chapter 1

Introduction

1.1. Motivation for Study

In 2023, the Clouds and the Earth's Radiant Energy System - Energy Balanced and Filled (CERES-EBAF) dataset – well-vetted and widely used for its radiative flux-focused information derived primarily from the Aqua and Terra satellite platforms – revealed the lowest global mean planetary albedo on record (Goessling et al. 2025), as well as a steady decline in global mean planetary albedo between 2000 and 2023 (Figure 1.1). Negative anomalies over broad swaths of ocean were a particularly significant contributor, with the strongest signals appearing over the Central Indian Ocean, the Atlantic Ocean off the Northwest Coast of Africa, and a large expanse of the North Pacific Ocean (Figure 1.2). As oceans that do not contain sea ice are generally poor

reflectors of incoming solar radiation – and, in fact, are consistently and reliably *absorbent* surfaces (Perovich 2018, Duspayev et al. 2024) – it is reasonable to consider clouds as the main drivers of these negative anomalies, due to their prominent presence over oceans and their nature as known, strong reflectors of solar radiation in the climate system (Chen et al. 2014, Zhan and Liang 2022, Zhang and Feingold 2023). Additionally, the sudden dip of ~0.6% in global mean albedo occurring mid-year in 2023 shown in Figure 1.1 further supports the likelihood of clouds being an appreciable source of the year's overall low albedo, since clouds are highly ephemeral and variable; a sudden change in spatial coverage or unusual bias toward less reflective clouds yields an instantaneous impact on mean albedo (George and Wood 2010, Bender et al. 2016, L'Ecuyer et al. 2019).

On average, clouds demonstrate a net cooling effect on the planetary system and make up ~50% of Earth's albedo (Mueller et al. 2011), making them not only crucial but an overwhelmingly dominant component in the climatological radiative energy balance (Ramanathan et al. 1989, Trenberth et al. 2009, Liu et al. 2011, Matus and L'Ecuyer 2017, Hang et al. 2019). Therefore, obtaining long-term estimates of cloud albedo and related parameters – such as cloud fraction – is necessary to accurately monitor changes in Earth's climate. Various studies have used climate models to infer temporal trends in energy balances and related quantities (Taylor et al. 2007, Qu et al. 2014, Goessling et al. 2025), but the accuracy of these investigations is restricted by the limitations posed by clouds. Since clouds often have a smaller spatial extent than the resolution of most available climate models can accommodate, their presence is necessarily accounted for by the implementation of physical parameterizations (Lopez 2007, Klein et al. 2013). This inevitably introduces uncertainty in the contribution of clouds to the climate system as well as any parameter pertaining to the cloud radiative effect.

As an alternative, observational data provided by satellites can be used either supplementally or exclusively in order to better capture the role of clouds in long-term analyses of albedo, energy balances, and related products (Lattanzio et al. 2013, He et al. 2014). It is easy to assume that the CERES-EBAF record would be a sufficient candidate for this purpose. However, though it is reliable for general analysis of energy balances, that reliability degrades in the case of specific, cloud-based analysis. While CERES-EBAF supplies data for cloud properties such as area fraction, optical depth, effective pressure, and effective temperature, attempts to use these properties for investigation are hindered depending on the nature of their application. For instance, analyses attempting to make use of cloud optical depth (COD) can be significantly impacted by the limited range of possible measurements (~0.05–53.2), which can exclude both the thinnest and the thickest clouds from study. A similar phenomenon is observed in analyses attempting to use cloud effective pressure; both the highest and the lowest-level clouds are excluded from study (Figure 1.3). Furthermore, if a study's objective relies on the capability of a record to sort clouds into individual type bins based on level and optical depth, CERES-EBAF falls short on account of the fact that it *only* provides effective pressure – not cloud top pressure (CTP), which is necessary for accurate cloud typing, per the International Satellite Cloud Climatology Project (ISCCP) cloud-type map (Figure 1.4) (Rossow and Schiffer 1999).

Therefore, a study aiming to determine the role of clouds in the declining global mean planetary albedo and its associated record-low in 2023 necessitates the use of a separate dataset which provides the fullest range of information possible on clouds and their physical properties. This thesis proposes the use of the Pathfinder Atmospheres-Extended (PATMOS-x) cloud climate record for this purpose.

1.2. Overview of PATMOS-x

PATMOS-x is a multidecadal climate data record (CDR) that provides data for a vast array of measurements and derived cloud products from 1980-present and is comprised of retrievals from NOAA's polar-orbiting environmental satellites (POES), numbered -06 through -19, as well as EUMETSAT's METOP polar orbiters -A, -B, and -C (Foster et al. 2023). Each of these sixteen satellites flies the Advanced Very High-Resolution Radiometer (AVHRR), which offers 4-6 spectral channels dependent upon the generation of the instrument. NOAA-06, -08, and -10 flew the four-channel AVHRR/1, NOAA-07, -09, -11, -12, and -14 flew the five-channel AVHRR/2, and all subsequent satellites in the record flew, or currently fly, the six-channel AVHRR/3. However, the AVHRR/3 can only operate five channels at a time, requiring a selection of either Channel 3a or 3b according to mission objectives (Heidinger et al. 2014).

In an investigation related to cloud albedo, data recorded by AVHRR Channel 1 – which measures in the visible reflectance band, centered at 0.65 μm – is most pertinent. Although visible reflectance is not an exact measure of albedo, it *is* still a measure of reflected solar radiation, making it a sufficient analogue for approximating the relative contribution of clouds to the planet's reflective efficiency and how that contribution may be changing over time both globally and regionally. Since the AVHRR does not feature onboard calibration for Channel 1, visible reflectance data must be vicariously calibrated to ensure measurement accuracy (Heidinger et al. 2002, Bhatt et al. 2016). Calibration of an individual AVHRR is frequently performed according to the procedures of the stable target method (Nagaraja Rao and Chen 1996, Loeb 1997). This method is implemented by comparing AVHRR reflectance time series of known, radiometrically stable Earth targets, such as deserts (Kaufman and Holben 1993, Heidinger et al. 2003), ice sheets (Loeb 1997), or bright clouds (Doelling et al. 2004, Sohn et al. 2009) against a reflectance time

series of those same targets from a well-calibrated platform like the Moderate Resolution Imaging Spectrometer (MODIS). This comparison is then used to derive a set of coefficients, the corrective application of which accounts for post-launch, time-dependent sensor degradation (Heidinger et al. 2002, Vermote and Saleous 2006).

PATMOS-x, however, is a special case regarding its calibration methodology. Its calibration is innately complicated by its intended use as a climate record. AVHRR is a competent sensor for real-time observational measurements, but it was never intended for use in climatological analyses spanning multiple decades; agreement between satellites is crucial, yet the standard stable target calibration method for *individual* AVHRR sensors cannot adequately bring measurements from all sixteen satellites featured in PATMOS-x into alignment with one another (Heidinger et al. 2010). Since 2010, the calibration of PATMOS-x visible reflectance has been derived and frequently updated with an inter-sensor approach. At present, while the record's intercalibration does build off prior stable target-based methodology, it is primarily composed of simultaneous nadir overpass (SNO) comparisons with MODIS and other AVHRR sensors, which relies on the evaluation of scenes viewed near-directly overhead by more than one satellite platform at the same time to derive corrective coefficients that ultimately allow for better inter-sensor agreement (Foster et al. 2023).

Other complicating factors of using PATMOS-x visible reflectance arise from differing local overpass times (LOTs), as well as each satellite's tendency to drift out of its original orbit (Norris and Evan 2015, Ackerman et al. 2019, Bojanowski and Musiał 2020); the degree to which this drift occurs and impacts radiometric retrievals varies from platform to platform (Foster and Heidinger 2013) and can be observed in Figure 1.5. Measurement disagreements that occur as a result of LOT differences and orbital drift are a function of solar zenith angle (SZA) and encompass

a separate issue that is not handled by the calibration procedure (Nagol et al. 2014, Bhatt et al. 2016); the objective of calibration is only to mediate the effects of natural sensor degradation over time. An additional SZA-based normalization must be applied to the reflectance data post-calibration in order to resolve the added inaccuracies arising from drift and mismatch between LOTs. In PATMOS-x, a standard μ-normalization is applied to visible reflectance, wherein reflectance is divided by the cosine of its respective SZA. However, Figure 1.5 demonstrates that this normalization is an inadequate resolution for drift and LOT impacts; this is because the μ-normalization relies on the Lambertian assumption that all targets reflect radiation equally in all directions, which is an inappropriate assumption to make in a real-world observational context (Lorente et al. 2018, Bacour et al. 2020). A method revising PATMOS-x's pre-applied normalization is outlined in Chapter 2. Undeniably, there are challenges presented in using PATMOS-x for analyses of visible reflectance, but this only means the correct steps – outlined in the following section – must be taken to ensure the retrieval of reasonably accurate estimates.

1.3. Statement of Research Objectives

The overarching objective of this thesis is to determine the efficacy of using the PATMOS-x record for global analysis of cloud contributions to planetary albedo via analogous assessments of visible reflectance. To do this, the record's most recent intercalibration must be validated, the process of which certifies that the effects of sensor degradation on data accuracy across all platforms are sufficiently captured and resolved. The validation procedure involves the use of tropical deep convective clouds (DCCs) as climatologically predictable targets to evaluate the stability of reflectance measurements over time and is detailed at-length in Chapter 2. This is a novel method of validation in the context of PATMOS-x, since the record's intercalibration,

while incorporating stable target principles, has never been derived with DCCs as stable targets; the introduction of DCC-based methodology ensures that the effectiveness of the intercalibration already established with prior stable target principles and SNO comparisons can also be observed from an entirely independent perspective. Embedded in this validation exercise is the development of an improved SZA normalization to take the place of the pre-existing μ-normalization, the steps of which are presented in Chapter 2.3.

Once it is verified that (a) the intercalibration is adequate for capturing sensor degradation impacts, and (b) the newly-developed SZA normalization amply corrects for further impacts from LOT differences and drift, a new product – cloud effective reflectance (CER) – will be derived in Chapter 3 to best approximate the relative reflective contribution of clouds on both a global and regional scale. CER is an important distinction from unweighted cloud visible reflectance, as it accounts for the fact that not all cloud types are equally reflective, nor are they equally as common; CER weights each cloud type by its relative prevalence of occurrence in the climate system to obtain a more accurate representation of individual cloud type contribution. The results of the time series and map-based CER analyses will then be compared against those of CERES-EBAF planetary albedo to assess the performance of PATMOS-x in a broad, global context, as well as a narrower regional context. If PATMOS-x agrees well with a known, reliable dataset like CERES-EBAF, therein lies the implication that, at least under certain conditions, it can be acceptably used in climatological investigations of visible reflectance and visible reflectance derivatives.

Below are the explicit research questions this thesis seeks to address:

Is PATMOS-x a viable dataset for investigating global cloud effective reflectance?

- *Does the record's radiometric intercalibration adequately resolve the effects of time-dependent sensor degradation?*
- *Does the new SZA normalization methodology adequately remove uncertainties due to orbital drift and LOT differences?*
    - *Is this normalization methodology applicable when the scope of analysis is broadened beyond tropical DCCs?*
- *Does PATMOS-x cloud effective reflectance agree well with CERES-EBAF planetary albedo?*
    - *If so, under what conditions is this agreement observable?*

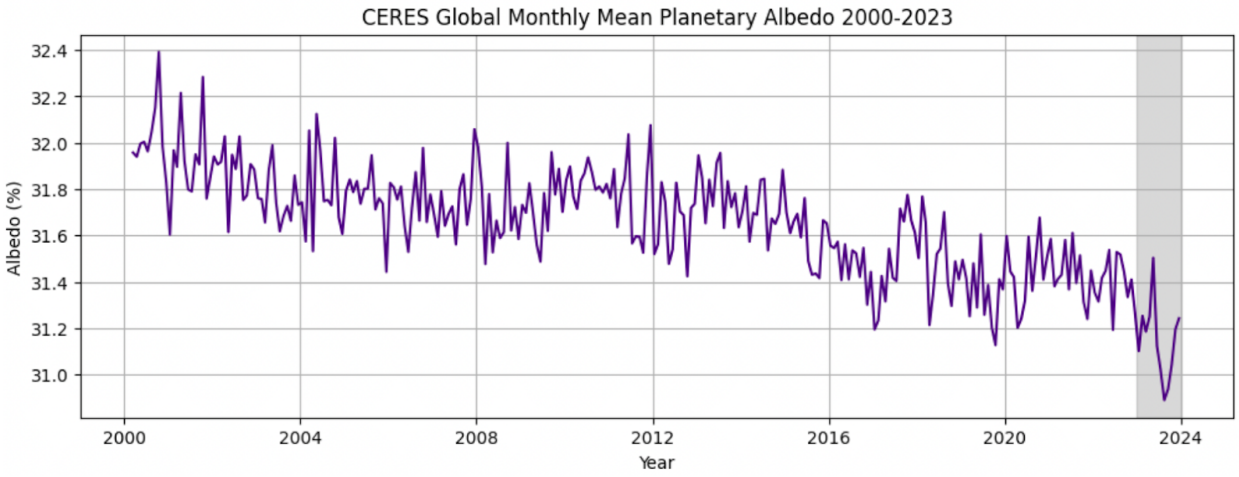

Figure 1.1: CERES-EBAF global monthly mean planetary albedo time series from 2000 to 2023, demonstrating an overall 23-year decline in albedo with a record low mid-year in 2023. Albedo is computed as the ratio of outgoing shortwave radiation to incoming shortwave radiation and weighted by the cosine of the latitude. It is then deseasonalized to eliminate the impacts of cyclic seasonal oscillations. The gray shading highlights the months of 2023.

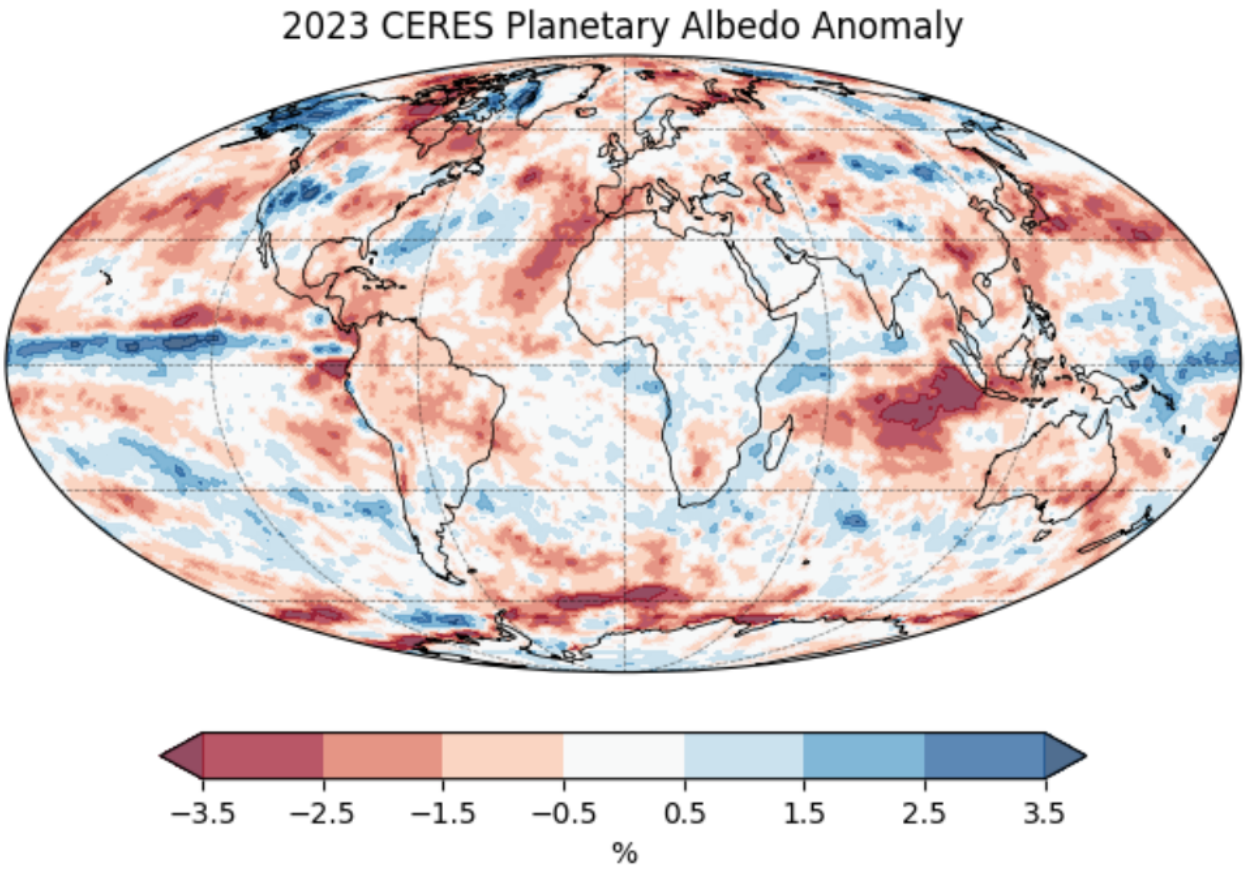

Figure 1.2: Global map of CERES-EBAF planetary albedo anomaly in 2023. Negative anomalies are particularly prevalent over the Central Indian Ocean, North Pacific Basin, and off the coast of Northwest Africa. El Niño-related increased convective activity in the Eastern Equatorial Pacific is also indicated.

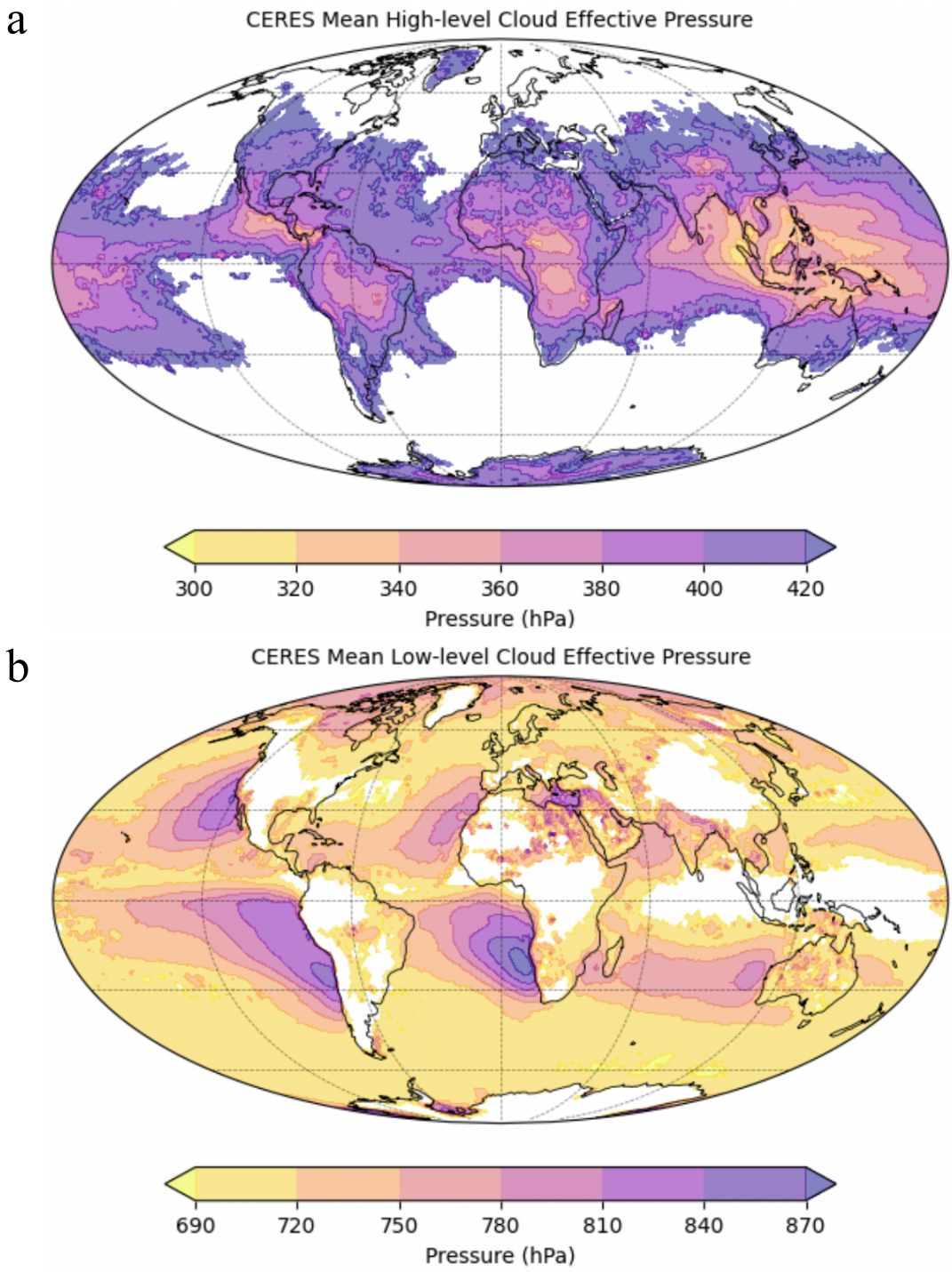

Figure 1.3: Global maps of CERES-EBAF (a) mean upper-level cloud effective pressure and (b) mean low-level cloud effective pressure. In both cases, clouds are not properly accounted for in large regions of the world as a result of the excessively narrow range of effective pressures. There is a misleading implication that upper-level clouds only exist within the middle latitudes and over ice-covered land surfaces, and that low-level clouds do not exist at all over regions where their presence would still be expected.

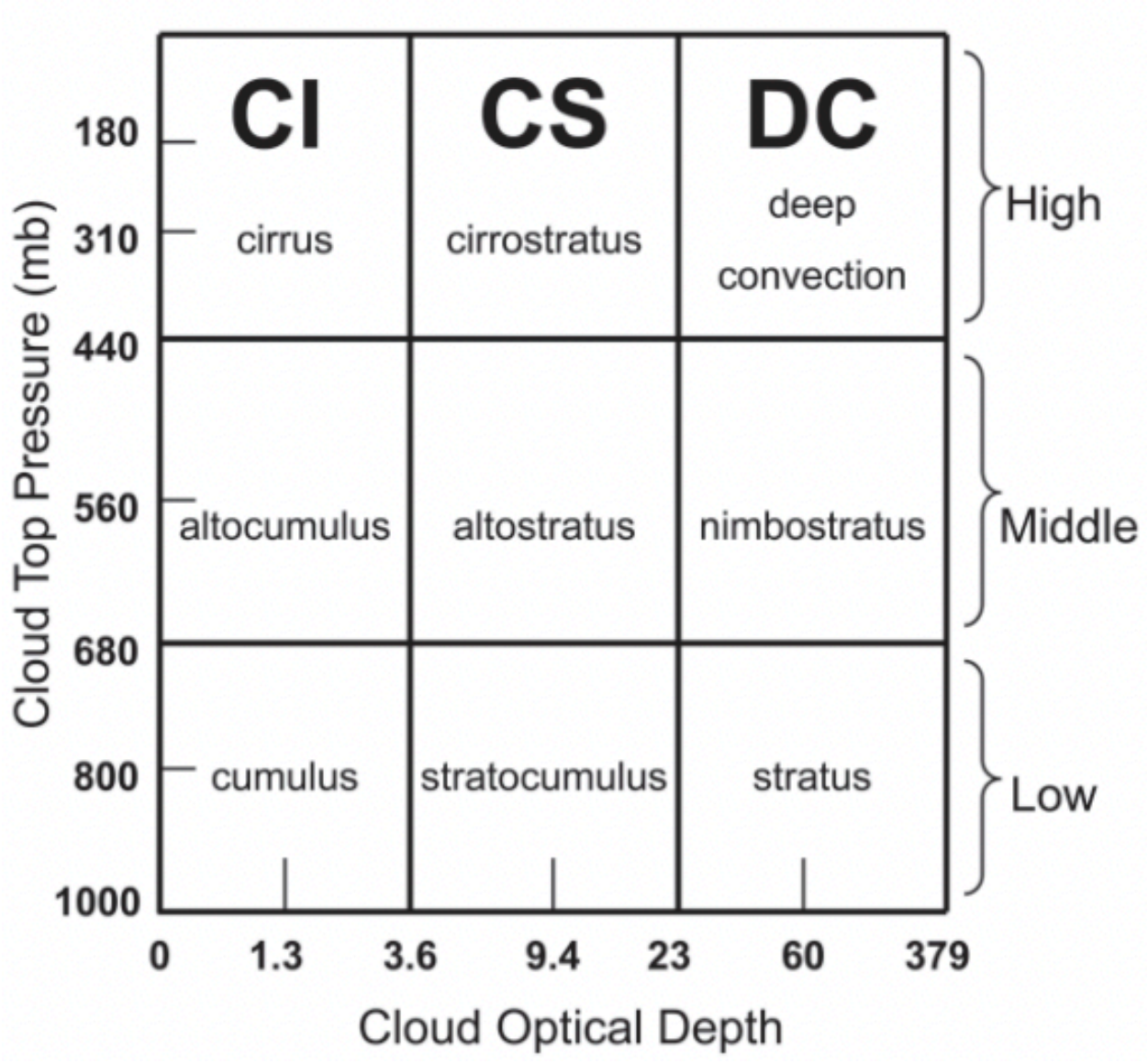

Figure 1.4: ISCCP cloud type map presented in Rossow and Schiffer (1999) and Wu and Kau (2007). Cloud types are binned by cloud top pressure (CTP) and cloud optical depth (COD) and assigned classifications based on known microphysical properties and climatological observations.

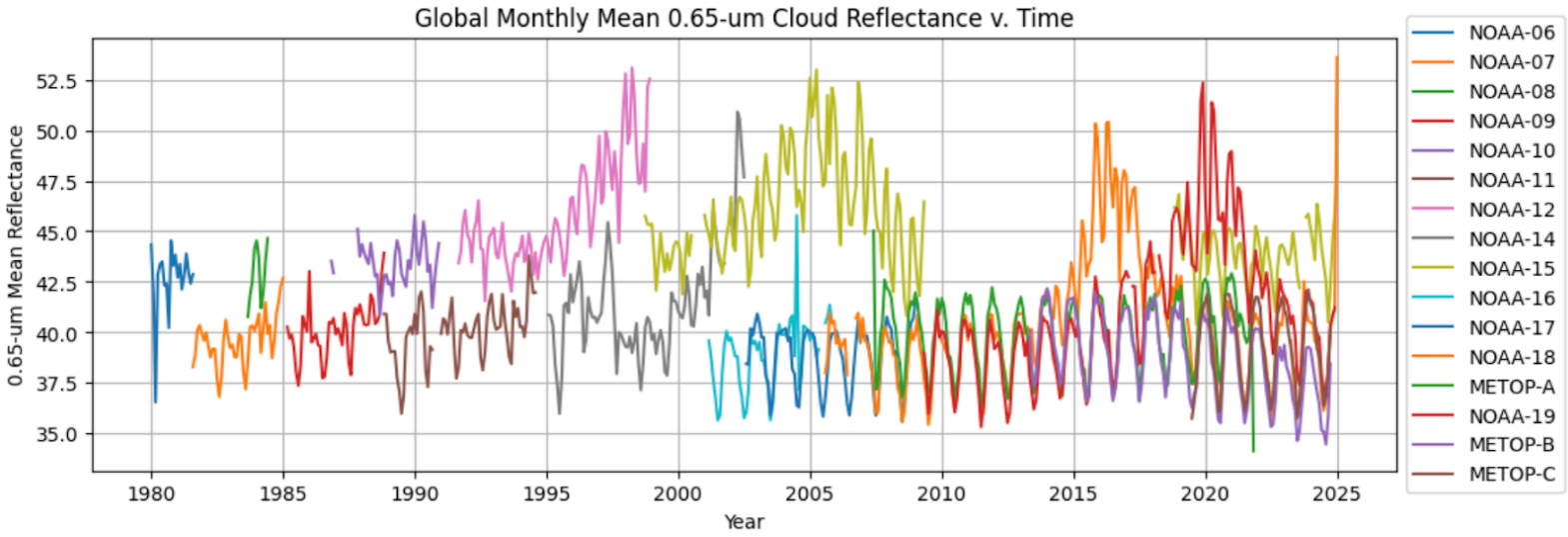

Figure 1.5: PATMOS-x Channel 1 global monthly mean cloud reflectance over time, parsed by individual satellite platform, from 1980 through 2024. Each satellite presents varying degrees of orbital drift and inter-sensor discontinuity from local overpass differences that are not resolved by the pre-applied μ-normalization. Seasonality also becomes especially noticeable in the latter half of the record.

Chapter 2

Calibration Validation Using Tropical Deep Convective Clouds

2.1. Data and Methods Overview

The primary dataset used for all analyses performed in Chapters 2 and 3 is the PATMOS-x Level-2bc CDR. It is sampled at a 1.0º x 1.0º spatial resolution with an ascending node file and descending node file for each day from 1980-present. The record from which it is derived is PATMOS-x Level-2b, sampled at a 0.1º x 0.1º resolution – 100-times the size of Level-2bc. Use of Level-2bc is strategic in the sense that the coarser resolution allows for better ease of processing and computation without compromising the overall accuracy of data retrievals,

particularly in time series analysis; to that effect, Level-2b is best suited for spatial mapping of data, while Level-2bc is ideal for identifying long-term climatological patterns of behavior.

In this chapter, Channel 1 0.65-µm visible reflectance of tropical DCCs will be evaluated over time to evaluate the reliability of the most recent PATMOS-x intercalibration. This will be presented through a succession of steps: (a) selection of raw 0.65-µm tropical DCC reflectance counts with the application of several filters, (b) conversion of counts to reflectance with a set of count-to-reflectance (CtR) equations, (c) plotting of the pre-normalized reflectance over SZA to obtain a set corrective coefficients, (d) normalization of the reflectance to a SZA of 20º using those corrective coefficients, and (e) computation of the monthly mean reflectance and plotting of a time series. If the monthly mean time series of DCC reflectance appears flat and stable, with a maximum uncertainty range of ~4%, the PATMOS-x intercalibration will be deemed sufficient for handling the effects of sensor degradation.

While 4% is a seemingly arbitrary threshold, it must be considered from the standpoint of MODIS as a reference. MODIS retrievals are considered well-calibrated because MODIS possesses the ability to continuously recalibrate itself rather than having to rely on post-retrieval vicarious calibration (Heidinger et al. 2002; Xiong et al. 2018). As a result, the MODIS uncertainty threshold is capped at a narrow ±2%, meaning the total uncertainty range is ~4%; this threshold is presently the gold standard for a well-calibrated CDR, thus setting the ideal uncertainty range for AVHRR retrievals at ~4% as well.

Finally, an additional step will be taken to solidify the conclusion of the calibration validation: the ISCCP-Next Generation (ISCCP-NG) Level-1g demo dataset – described in further detail in Section 2.3 – will be used to select tropical DCC reflectances with the same filtering criteria from step (a) in the PATMOS-x validation procedure. The DCC reflectance points will be

plotted over SZA as in step (c) of the validation, then the associated fit line will be compared against that of PATMOS-x. By incorporating a comparison of the PATMOS-x SZA normalization fit to that derived from a known, well-calibrated dataset, the confidence with which conclusions can be drawn about the PATMOS-x intercalibration's ability to resolve sensor degradation impacts as expected is significantly increased.

2.2. Count-to-Reflectance Conversion

The PATMOS-x visible reflectance intercalibration is applied through a conversion relationship between the pre-calibrated unitless integers recorded by the AVHRR sensor – termed "counts" – and the resultant top-of-atmosphere (TOA) reflectance. In order to perform the conversion, the following variables must be given for each satellite: launch date, from which the amount of time elapsed since launch is derived, and the set of three calibration coefficients obtained from the intercalibration process. The equations incorporating these variables are given below:

$$G = \frac{S_1(100 + S_2\Delta t + S_3\Delta t^2)}{100} \quad (2.1)$$

$$R = G \bullet C \quad (2.2)$$

$$D = 1 - 0.016729\cos\left(\frac{0.9856\pi d}{180}\right) \quad (2.3)$$

$$R_f = R \bullet D^2 \quad (2.4)$$

Where G is the calculated gain, S_1, S_2, and S_3 are the empirically-derived calibration coefficients, Δt is the time elapsed since launch date, R is the initial reflectance, C is the reflectance count, D is the Sun-Earth distance adjustment factor to account for seasonal changes in reflectance as a natural

consequence of Earth's elliptical orbit, d is the day of year, and R_f is the final converted and adjusted reflectance.

It is important to note that this series of equations is the product of an important modification that has been made to the general conversion method to correctly handle gain disparities between AVHRR generations. All satellites flying the AVHRR/1 and AVHRR/2 return single-gain measurements. However, all satellites flying AVHRR/3 – NOAA-15 and beyond – return dual-gain measurements. The original conversion equations incorporate the "dark count" – the minimum count value at which a measurement can be recorded – and "switch count" – the count value at which a sensor shifts from measuring in a low-gain mode to a high-gain mode – to accommodate dual-gain sensors. Due to the fact that the early half of the PATMOS-x record encompasses measurements taken from single-gain sensors, the original conversion equations cannot be used. Therefore, equations 2.1-2.4 above are designed to treat all reflectance count measurements as if they were recorded by a single-gain sensor. This works *only* when the calibration coefficients for dual-gain satellites are scaled with adjustment factors to equate the low-gain coefficients with the high-gain coefficients, which negates the need to account for a dark or switch count; low-gain coefficients are divided by a factor of 0.5 and high-gain coefficients are divided by a factor of 1.5.

With this modification made to dual-gain calibration coefficients, the CtR procedure is performed on reflectance counts for DCCs. DCC counts are selected by imposing a set of conditions: brightness temperature (T_b) < 200 K to obtain only the coldest cloud tops (often overshooting), SZA < 80º to avoid including samples close to the solar terminator (neglecting to do this can introduce excessively dark pixels into the eventual mean calculation and skew results), and Sensor / Platform Zenith Angle (PZA) < 15º to mitigate undue 3D shadowing effects. Such

effects are still present, but they are not as prevalent at near-nadir angles as they are at oblique viewing angles, where the sensor cannot capture the highest intensity backscatter. Finally, DCC samples are limited between 20º S and 20º N, as deep convective cells in the Tropics are more physically consistent; they tend to be taller, more optically thick, and therefore brighter, which makes them ideal targets for stable target evaluation.

Inputting the tropical DCC counts into Equations 2.1-2.4 and generating a scatterplot time series parsed by individual satellite yields the result shown in Figure 2.1. The assumption at this point is that the reflectance values shown are calibrated. However, this cannot be properly corroborated due to the significant presence of orbital drift – particularly in the pre-2000 platforms and NOAA-18 and -19 – and local overpass discontinuities.

2.3. Solar Zenith Angle Normalization

The reflectance resulting from the CtR conversion is not normalized. To obtain the same values presented by the pre-existing PATMOS-x 0.65-µm reflectance variable, the converted reflectance would be divided by the cosine of the solar zenith angle (μ). However, since the lacking ability of this corrective normalization to resolve SZA-based phenomena has already been established, the normalization that must be applied to the converted tropical DCC reflectance requires revision.

The following SZA normalization methodology relies on the known relationship between SZA and measured reflectance but does *not* rely on the assumption that all DCC targets are isotropic reflectors. Converted DCC reflectance from all satellites is plotted against SZA and is fit with a simple 2nd-degree polynomial line in Figure 2.2, which demonstrates an explicit correlation

of reflectance to SZA – in general, the greater the SZA, the darker the measured reflectance; the lower the SZA, the greater and more physically appropriate the reflectance is.

Taking the fit line equation:

$$R = -0.006952686790^2 - 0.6501460630 + 105.468679 \quad (2.5)$$

Where R is the converted reflectance and θ is the SZA, a series of computational steps can be performed to retrieve reflectance normalized to SZA = 20º:

$$R_{20} = C_1(20)^2 + C_2(20) + C_3 \quad (2.6)$$

$$R_\theta = C_1\theta^2 + C_2\theta + C_3 \quad (2.7)$$

$$R_{offset} = R_{20} - R_\theta \quad (2.8)$$

$$R_{normalized} = R_{pre-normalized} + R_{offset} \quad (2.9)$$

Where R_{20} is the converted reflectance at SZA = 20º, C_1, C_2, and C_3 are the coefficients from Equation 2.5, R_θ is the reflectance array across all SZAs, R_{offset} is the magnitude that R_θ deviates from reference reflectance R_{20}, and $R_{normalized}$ is the final reflectance normalized to SZA = 20º obtained from adding the offset back to the pre-normalized converted reflectance. Converted reflectance is normalized to 20º so that the final resulting reflectance most accurately captures the expected reflective behavior of DCCs.

Figure 2.3 shows a scatterplot time series of tropical DCC reflectance that has been normalized with the application of Equations 2.6-2.9. When compared against the pre-normalized reflectance time series (Figure 2.1), a marked improvement in measurement stability is observed

over time; there appear to be no significant LOT discontinuities between satellites, and orbital drift is largely resolved. Before the final mean calculation is made, however, an intermediate step is performed to ensure the reflectance-SZA fit line characterized by Equation 2.5 does not contain any significant *unresolved* sensor degradation impacts that should've been handled by the intercalibration.

This intermediate step involves the aforementioned ISCCP-NG Level-1g demo dataset, which compiles data from all geostationary imagers from 2021 and 2022 at a 30-minute interval and a maximum of a 4-km equirectangular grid resolution. All satellites in this dataset feature onboard continuous calibration and are therefore considered reliably well-calibrated. Using the same filtering criteria explained in Section 2.2, with an added minimum boundary for SZA of 20º, 0.65-µm tropical DCC reflectance is selected; this minimum SZA boundary is important, because the nature of Level-1g as a geostationary-based dataset means there are significantly more samples that are taken at SZA < 20º, whereas the PATMOS-x Level-2bc dataset has very few samples taken at SZA < 20º. Applying the 20º minimum threshold for Level-1g allows for a more direct comparison to Level-2bc. Once the Level-1g DCC reflectance is selected with the proper filtering criteria, it is plotted over SZA and fit with a 2nd-degree polynomial.

Figure 2.4 shows the comparison between the PATMOS-x Level-2bc and the ISCCP-NG Level-1g DCC reflectance, complete with fit lines. There is remarkable agreement between the Level-1g fit and the Level-2bc fit, which suggests that the PATMOS-x intercalibration does a good job of eliminating sensor degradation impacts on visible reflectance. The fact that the observed relationship between reflectance and SZA for PATMOS-x is more-or-less congruent with that of a well-calibrated reference dataset like ISCCP-NG offers greater confidence in the robustness of the PATMOS-x intercalibration.

Finally, with a greater certainty that the intercalibration is performing as expected, the SZA-normalized tropical DCC reflectance is averaged at a monthly frequency and, again, plotted over time, parsed by satellite. Figure 2.5a presents the monthly mean DCC reflectance points as fairly stable between 1980 and April, 2024, with only slight (on the order of approximately <3%) remnants of orbital drift signals – a marked improvement from the appearance of drift signals up to and even exceeding 60% in Figure 2.1. Zooming in, Figure 2.5b shows that the vast majority of data points are centered around an all-time mean of ~89.5% and confined between 88 and 92%, meaning they fall within the desired maximum uncertainty threshold of 4%. Thus, it can be concluded that the PATMOS-x visible intercalibration is sufficient, and the record is likely usable in broader analyses involving 0.65-µm reflectance.

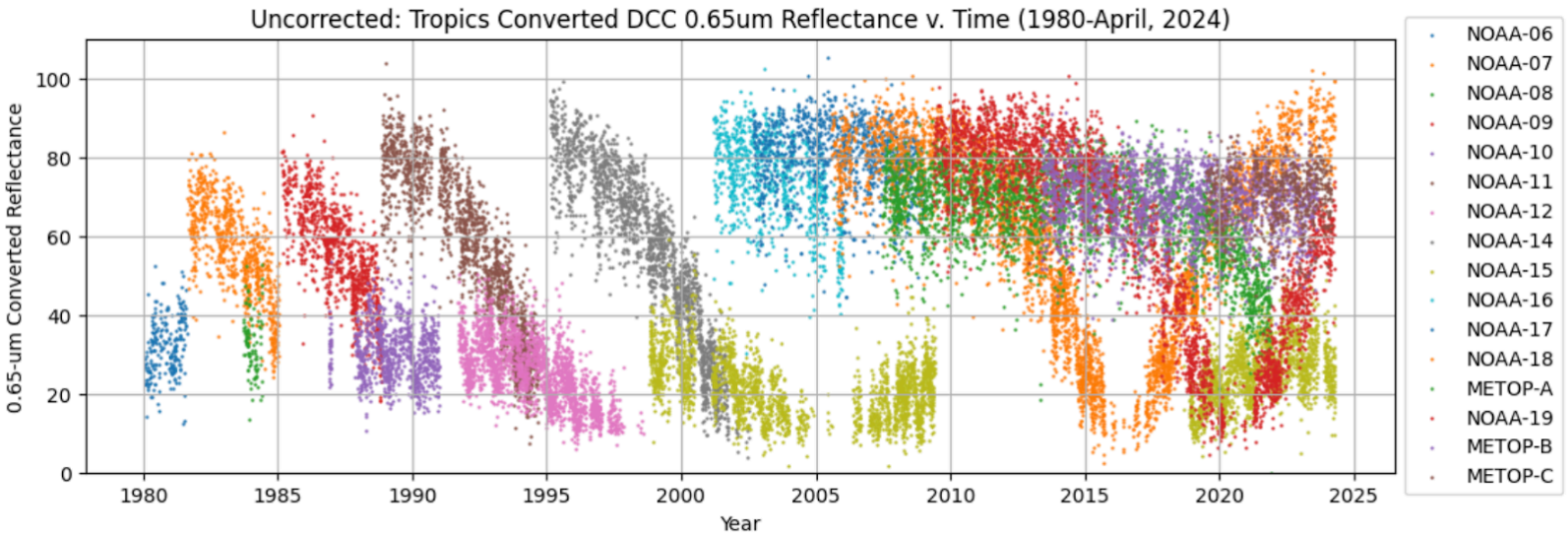

Figure 2.1: Pre-normalized converted tropical DCC reflectance from 1980 to April, 2024, parsed by individual satellite. Most platforms exhibit extreme orbital drift signals, and pre-2000 platforms show the largest discontinuities due to LOT differences.

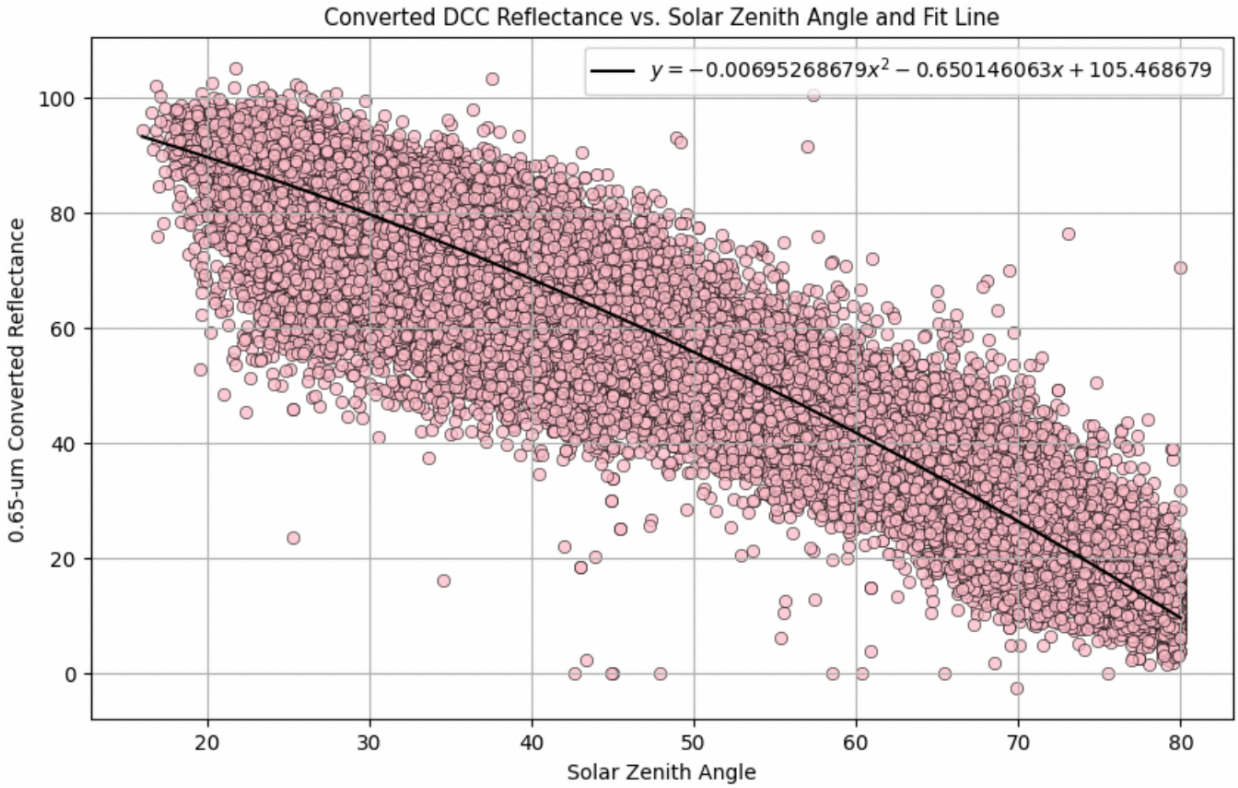

Figure 2.2: Scatterplot of pre-normalized converted tropical DCC reflectance over SZA, complete with 2nd-degree polynomial fit line. SZA is manually constrained to values < 80º and does not exceed a minimum of 10º. The plot includes data from all satellites.

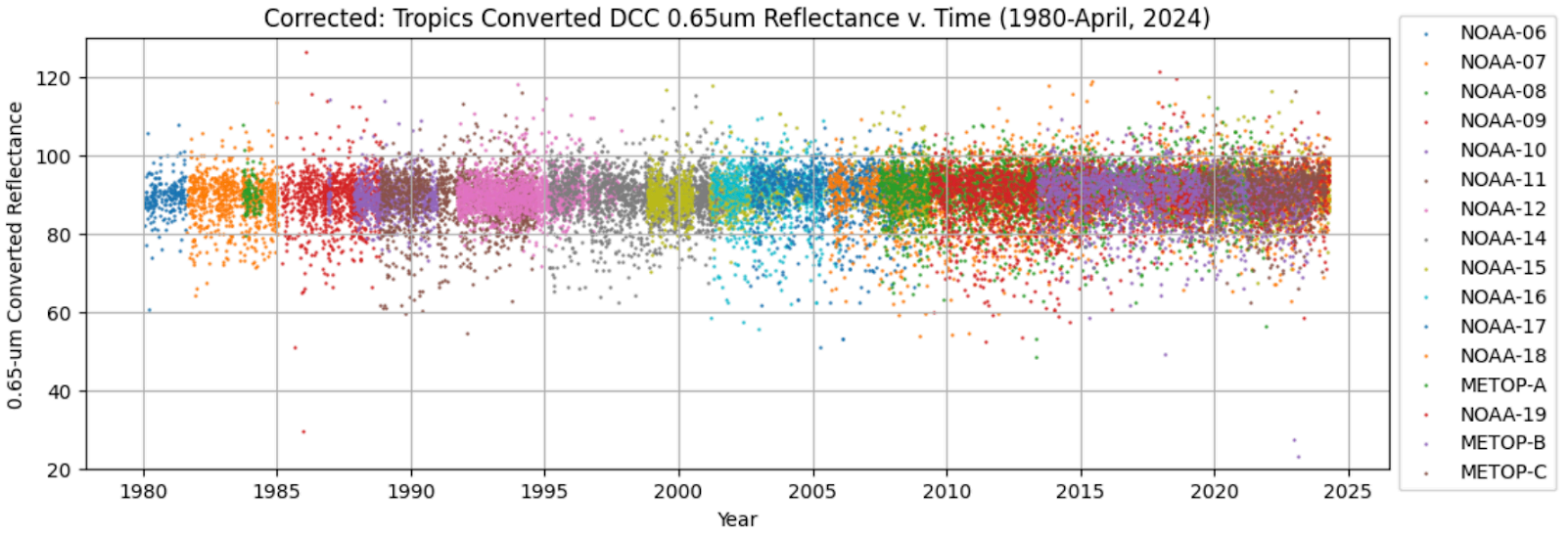

Figure 2.3: Converted tropical DCC reflectance from 1980 to April, 2024, parsed by individual satellite and normalized using the SZA-based relationship identified in Figure 2.2. Orbital drift signals and prominent discontinuities between satellites appear to be fairly well-resolved.

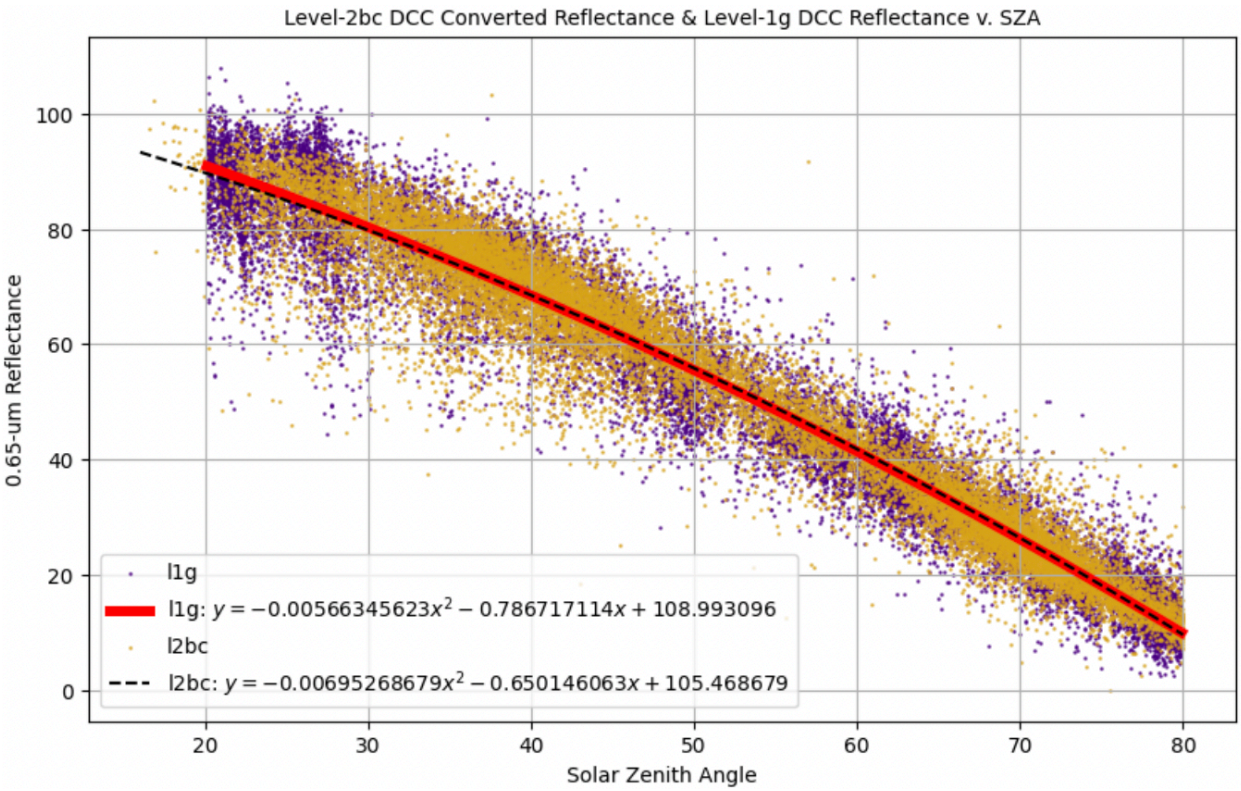

Figure 2.4: Scatterplot comparisons of PATMOS-x Level-2bc pre-normalized tropical DCC reflectance and ISCCP-NG Level-1g tropical DCC reflectance over SZA with respective fit lines. SZA for Level-1g is explicitly constrained between 20º and 80º to allow for a more direct comparison with Level-2bc.

a

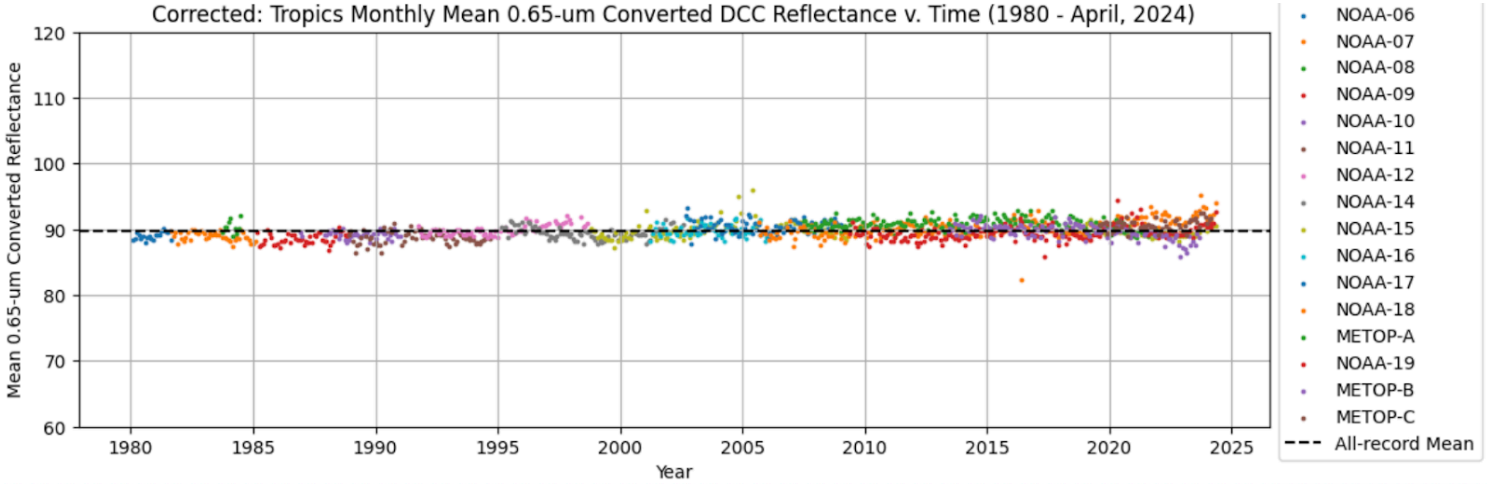

b

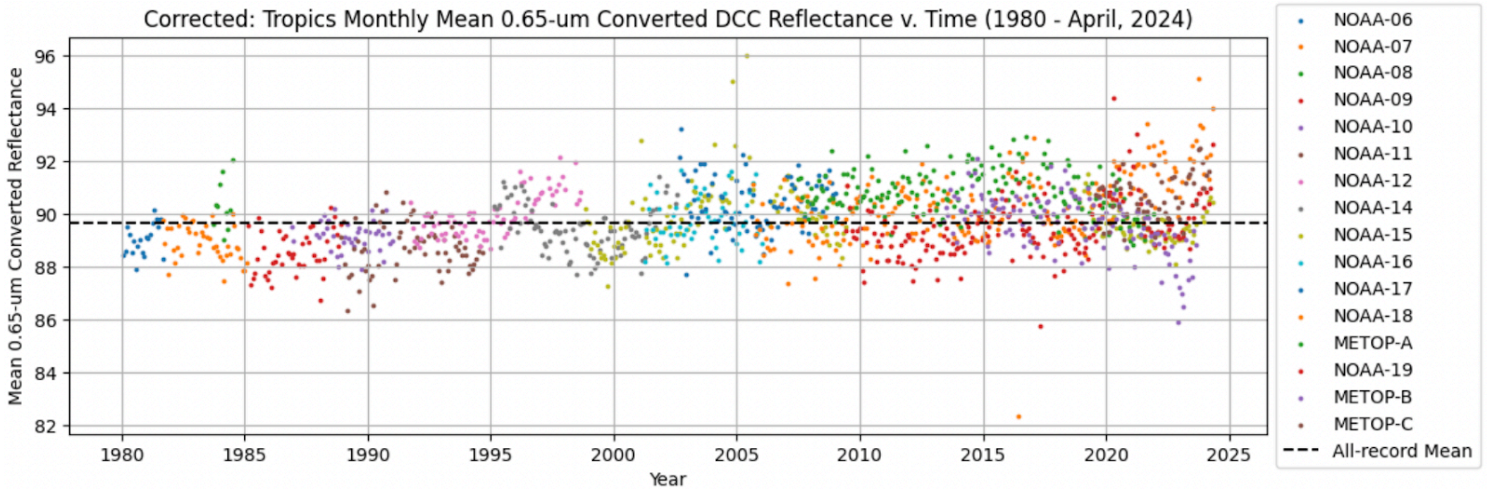

Figure 2.5: Scatterplot time series of SZA-normalized tropical DCC reflectance from 1980 to April, 2024 with (a) a zoomed-out perspective to assess measurement stability over time and (b) a zoomed-in perspective to determine uncertainty range. In both (a) and (b), the all-record mean is plotted as a horizontal dotted line at ~89.5%.

Chapter 3

Computation and Analysis of Cloud Effective Reflectance

3.1. Data and Methods Overview

Now that the validity of the PATMOS-x intercalibration has been established, an exercise in investigating the contribution of clouds to planetary albedo can be performed. To reiterate: with the identification of a 23-year downtrend in global planetary albedo and a record low occurring mid-year in 2023 by CERES-EBAF, and given that clouds account for ~50% of the planet's reflective potential, it is reasonably hypothesized that a change in cloud fraction is likely the most prominent driver of declining albedo. The following methodology and analysis therefore aim to use the PATMOS-x Level-2bc dataset to derive an analogous quantity to cloud albedo from 0.65-µm reflectance – cloud effective reflectance, described at length in Section 3.2 – and draw

up global monthly mean anomaly time series as well as map projections for 2023 of various cloud types and bins.

For final comparisons against CERES-EBAF, the temporal scope of analysis will be narrowed down to 2000-2023; however, for independent analyses of PATMOS-x performance, the full length of the record, starting in 1980, will be used. This serves the purpose of (a) determining how reliable the *entire* record can be for cloud reflectance analysis and (b) offering the potential of viewing pre-2000 trends in reflectance, which CERES-EBAF cannot do. Additionally, due to the relatively coarse resolution of Level-2bc, 2023 data from the PATMOS-x Level-2b record will be used as a supplement for map projections of 2023 cloud effective reflectance (CER) anomaly.

Ultimately, the overarching objective is to verify if PATMOS-x can be used for broad, global analysis of cloud effective reflectance. However, accessory regional analysis of the Central Indian Ocean will also be provided, complete with CERES-EBAF comparison, to contrast performance results between large and small-scale analysis scopes.

3.2. Global Cloud Effective Reflectance

As previously noted in Chapter 1.3, using the total unweighted cloud reflectance does not supply a proper analogue for cloud albedo. Some cloud types are more common and widespread in the climate system than others, but some cloud types that are *less* common are altogether more effective reflectors than those that are more common; this complexity is enshrined in the cloud fraction behavior of individual cloud types. In order to accurately approximate individual cloud type or bin reflective contribution, a new reflectance-based quantity that incorporates cloud fraction weights – CER – is computed. The mean of CER can be defined both spatially and temporally depending on the analysis category: time series or map visualization. In both instances,

the quantity returned is the result of dividing monthly 1.0º-gridded reflectance sums by the number of cloudy pixels (ensured with a filter of cloud probability (CP) > 0.5) and clear-sky pixels – more aptly-termed "all-sky" pixels. The division by the all-sky component is what encompasses the added effect of cloud fraction behavior.

The temporal and spatial equations for mean CER are provided below:

$$\overline{CER}_t = \sum_{\phi,\lambda} \left(\frac{\sum_c R(c,g,\phi,\lambda)}{\sum_c T(c,g,\phi,\lambda) + C(g,\phi,\lambda)} \right) \tag{3.1}$$

$$\overline{CER}_s = \sum_{c} \left(\frac{\sum_g R(c,g,\phi,\lambda)}{\sum_g T(c,g,\phi,\lambda) + \sum_g C(g,\phi,\lambda)} \right) \tag{3.2}$$

Where R is the reflectance sum for each month at each grid point, T is the valid cloud type pixel count, C is the valid clear-sky pixel count, g is the group (satellite-month pair) dimension, ϕ is the latitude dimension, λ is the longitude dimension, and c is the cloud type dimension. These equations are generalized to handle both all-cloud analysis and cloud type subset analysis.

Cloud types are determined according to the ISCCP cloud type map; however, a slight modification is made to the naming convention presented in Figure 1.4. Definitions are generalized simply by their level bin – high (CTP ≥ 680 mb), mid-level (680 < CTP ≤ 440 mb), and low (CTP < 440 mb) – and their COD bin – dark (COD ≤ 3.6), dim (3.6 < COD ≤ 23), and bright (COD > 23). The COD categories are derived from the relationship between the thickness of a cloud and its known reflective capability; thinner clouds are much less effective reflectors than thicker clouds. This modified naming convention is more descriptive of each cloud type's physical

characteristics and improves understanding of which types or bins are the most dominant contributors to reflective trends and anomalies.

The same SZA normalization methodology expressed in Chapter 2.3 is applied in the processing and cloud type sorting of 0.65-μm reflectance prior to summation for the mean CER calculations. Geometric filters applied across all cloud types are as follows: SZA < 80º and PZA < 30º. Since no CtR conversion is being performed for this phase of analysis, nor is it necessary, the pre-existing 0.65-μm reflectance variable stored in Level-2bc is used, with an added de-normalization step to eliminate the original standard μ-normalization: all reflectance values are multiplied by the cosine of their respective SZAs. Reflectance-SZA relationships are then derived for each of the three COD bins expressed above, rather than for each individual cloud type. This is because reflective characteristics of cloud types falling in the same COD bin are reasonably similar to one another. Generally speaking, dark clouds have a global mean reflectance range of ~5-15%, dim clouds ~30-45%, and bright clouds ~70-85% (Figure 3.1). Ideally, applying the same SZA normalization technique across all cloud types and across all latitudes would yield the same agreement between satellites observed in the tropical DCC validation.

In reality, however, individual cloud typing on a global scale introduces complications to the analysis at the normalization level. The attempt to derive the SZA normalization relationship for dark clouds, in particular, reveals a fault in an implicit assumption made while constructing the normalization methodology in Chapter 2.3: it is assumed that all clouds, across all optical depths are functionally opaque targets. Such an assumption is valid only for optically thick clouds (COD > 23). While the satellites can still correctly identify the presence of a dark cloud, cloud types falling into the COD < 3.6 bin are often thin enough to reveal the surfaces beneath them, and if those surfaces happen to be brighter than the clouds themselves, the sensor is more likely to record

the surface reflectance rather than the cloud reflectance. The result in plotting dark cloud reflectance over SZA is a branch of anomalously high reflectances that are unphysically bright for the cloud type (Figures 3.2d-f). This tendency of dark clouds to record underlying bright surface reflectances is significant enough to introduce a pronounced error and over-correction of reflectance values upon application of the fit line normalization.

Figure 3.2 visualizes this error, broken down to the three cloud types within the dark cloud bin. High-error reflectance points are defined as $E_R > 20\%$ off the mean reflectance-SZA curve. In Figures 3.2a and 3.2b, low-level dark clouds and mid-level dark clouds exhibit a significant concentration of these high-error points in and near the poles, which aligns with the suspicion that it is primarily thin cloud occurrences over bright surfaces like snow and sea ice that complicate the process of deriving the dark cloud bin reflectance-SZA relationship. This initially suggests that an additional filter can be applied to omit reflectance samples where clouds are detected over snow and ice, largely preventing high-error points from getting factored into the normalization and eventual mean calculation. However, Figure 3.2c shows that upper-level dark clouds feature a significant population of high-error points over deserts and large swaths of continental land masses, which eliminates the possibility of maintaining a fully global CER analysis with PATMOS-x.

The analysis is thus constrained to an oceans-only perspective. A filter is applied to remove all cloudy pixel reflectances over land masses, ephemeral water sources, and inland water sources. Inevitably, this will degrade the usefulness of the final comparison of PATMOS-x CER to CERES planetary albedo, but it is still important to evaluate the performance of the PATMOS-x record in a context broadened past a singular cloud type in a small latitudinal band of the globe. Oceans-only SZA relationships for each of the COD-based cloud bins are shown in Figure 3.3; most

notably, the relationship derived for the dark cloud bin (Figure 3.3a) no longer exhibits branching, unphysically bright reflectances. Temporal monthly mean CER is then computed with normalization using these SZA relationships, and the all-record climatological average is subtracted to return CER anomaly. The anomaly is further deseasonalized to remove the seasonality signals that become prevalent in more globally-oriented analyses.

3.2.1. PATMOS-x Time Series Analysis

Figures 3.4, 3.5, and 3.6 show global ocean CER anomaly time series for COD bins, level bins, and all cloud types, respectively, from 1980 to 2023. Overwhelmingly, the best agreement between satellites is demonstrated in the dark cloud case (Figure 3.4a); there are discontinuities between pre-2000 satellites, which is likely a feature of there typically being only one satellite flying at any given time as well as early-satellite susceptibility to orbital drift compared to later satellites. As well, some satellites consistently record lower CER than others. However, these discontinuities and disagreements are somewhat insignificant, as the anomaly range only spans ~1%; the scale on which inter-satellite disparities are occurring is fairly small. The dim (Figure 3.4b) and bright (Figure 3.4c) cases exhibit more severe disagreements. In both instances, there are obvious drift signals >2% still appearing in pre-2000 satellites, and similar – though less severe – behavior is evident in post-2000 satellites as well. This implies that the SZA normalization is not performing with the degree of adequacy previously observed in Chapter 2's DCC analysis.

Inter-satellite disparities only become more prevalent when CER is binned by level (Figure 3.5). Upper-level clouds (Figure 3.5a) show extreme discontinuities between satellites, particularly between NOAA-12 and NOAA-14, and stark disagreement between NOAA-18 and the rest of the platforms flying after 2020. The mid-level cloud case (Figure 3.5b) also contains orbital drift and

discontinuities, most distinctly between NOAA-14 and NOAA-16. As well, low-level clouds (Figure 3.5c) exhibit this same discontinuity between NOAA-14 and NOAA-16, and consistently lower CER in NOAA-16, -18, and -19, as opposed to NOAA-17 and the METOPs.

When CER is computed for all cloud types (Figure 3.6) to visualize the combined effect of all clouds on effective reflectance over time, many of the drift signals and disagreements identified in the constituent bins are inevitably present; in many instances throughout the record, the SZA-based artifacts are not resolved by factoring all cloud types into the mean anomaly. Strong drift signals still appear pre-2000, and the NOAA-14/NOAA-16 discontinuity persists.

3.2.2. Comparison of PATMOS-x to CERES-EBAF

Due to the inability of the SZA normalization to sufficiently resolve orbital drift signals and inter-satellite discontinuities, alongside the fact that the analysis was necessarily constrained to an oceans-only perspective, a direct comparison against CERES-EBAF planetary albedo cannot be performed. This is solidified in Figure 3.7, which plots the 2000-2023 inter-satellite all-cloud mean CER anomaly from PATMOS-x with the CERES-EBAF global planetary albedo anomaly. Anecdotally, it can be concluded that, after 2000, CER over the oceans does appear to follow the same general albedo downtrend observed by CERES, and based on the fact that many of the local maxima and minima observed by PATMOS-x coincide with those observed by CERES, it can be stated that, to some extent, clouds over the ocean do contribute at least partially to albedo changes. However, too many sources of uncertainty have been identified to confidently *quantify* the extent to which clouds have contributed to the albedo downtrend or the record low in 2023. Additionally, the CERES albedo curve factors clear-sky surface reflectance into its total calculation; since landmasses and ocean surfaces are not significantly variable on a month-to-month or year-to-year

basis, they tend to offset anomaly signals presented by clouds on a global basis unless those signals are especially prominent. Therefore, attempting to draw explicit, quantified conclusions from a comparison between CERES global all-sky albedo and PATMOS-x CER over oceans is not a particularly useful exercise.

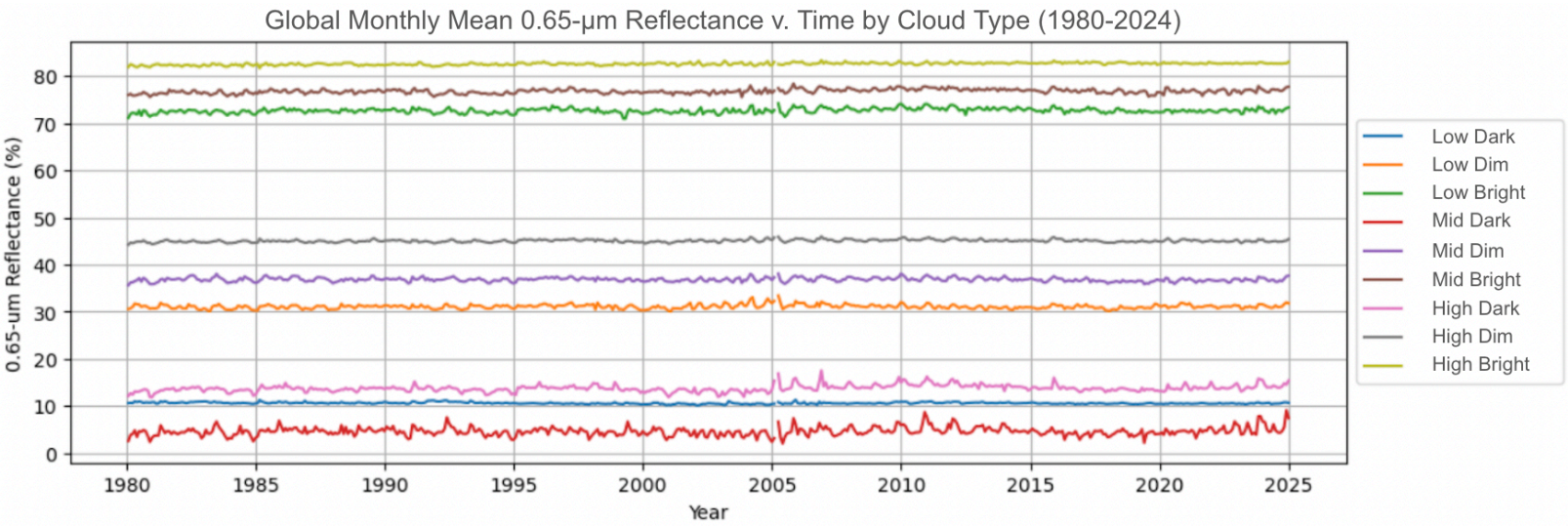

Figure 3.1: Global monthly mean 0.65-µm reflectance over time, parsed by cloud type from 1980 to 2024. Values are normalized using the SZA normalization methodology outlined in Chapter 2 and 3 and deseasonalized. There are three distinct groupings: dark clouds range from ~5-15%, dim clouds from ~30-45%, and bright clouds from ~70-85%.

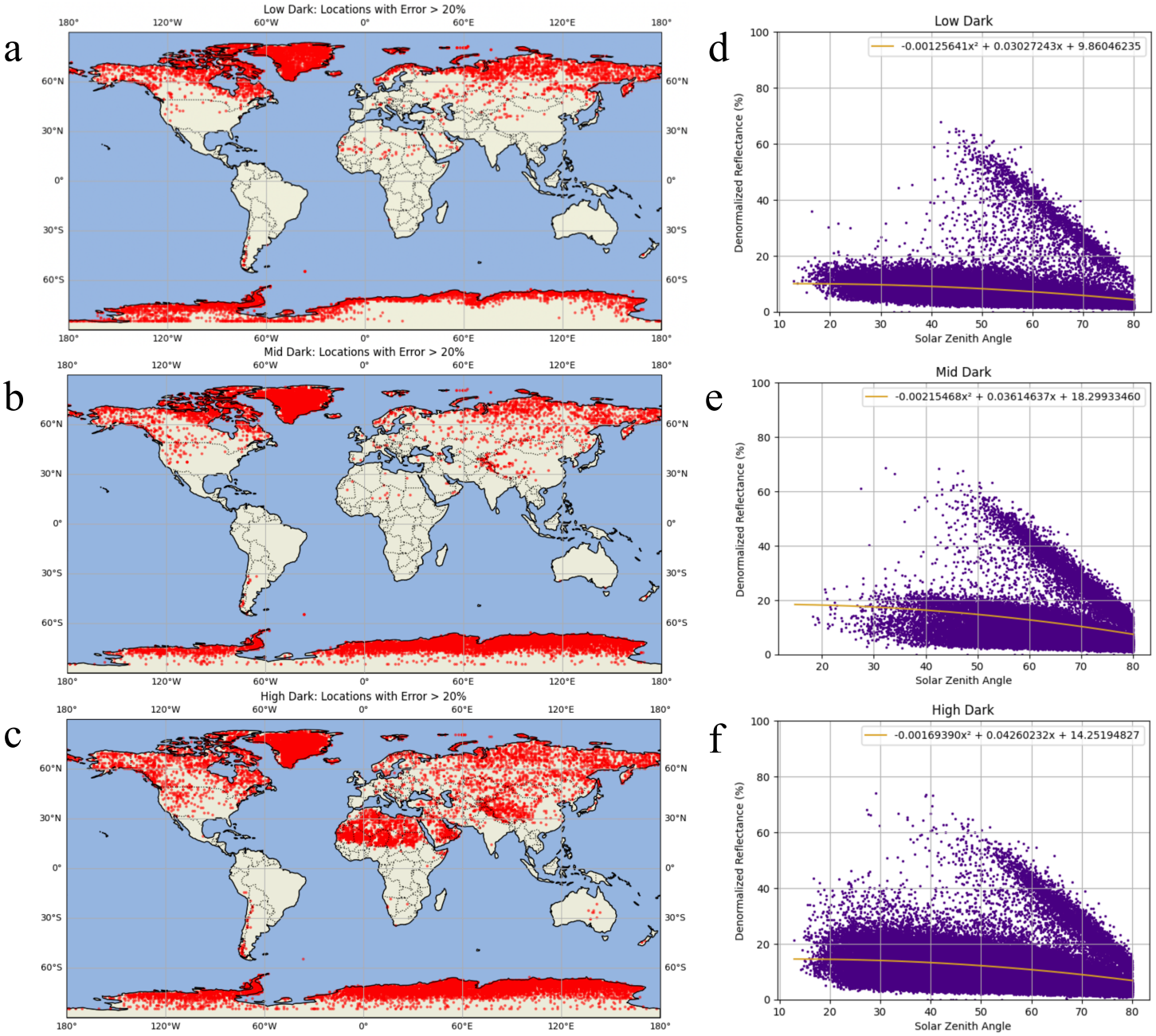

Figure 3.2: Map projections displaying the distribution of Reflectance Error > 20% points for dark clouds at the (a) low, (b) mid, and (c) upper levels, with associated reflectance-SZA scatterplots for (d) low, (b) mid, and (c) upper levels. Maximum SZA threshold is set at 80º, and the maximum PZA threshold is set to 30º.

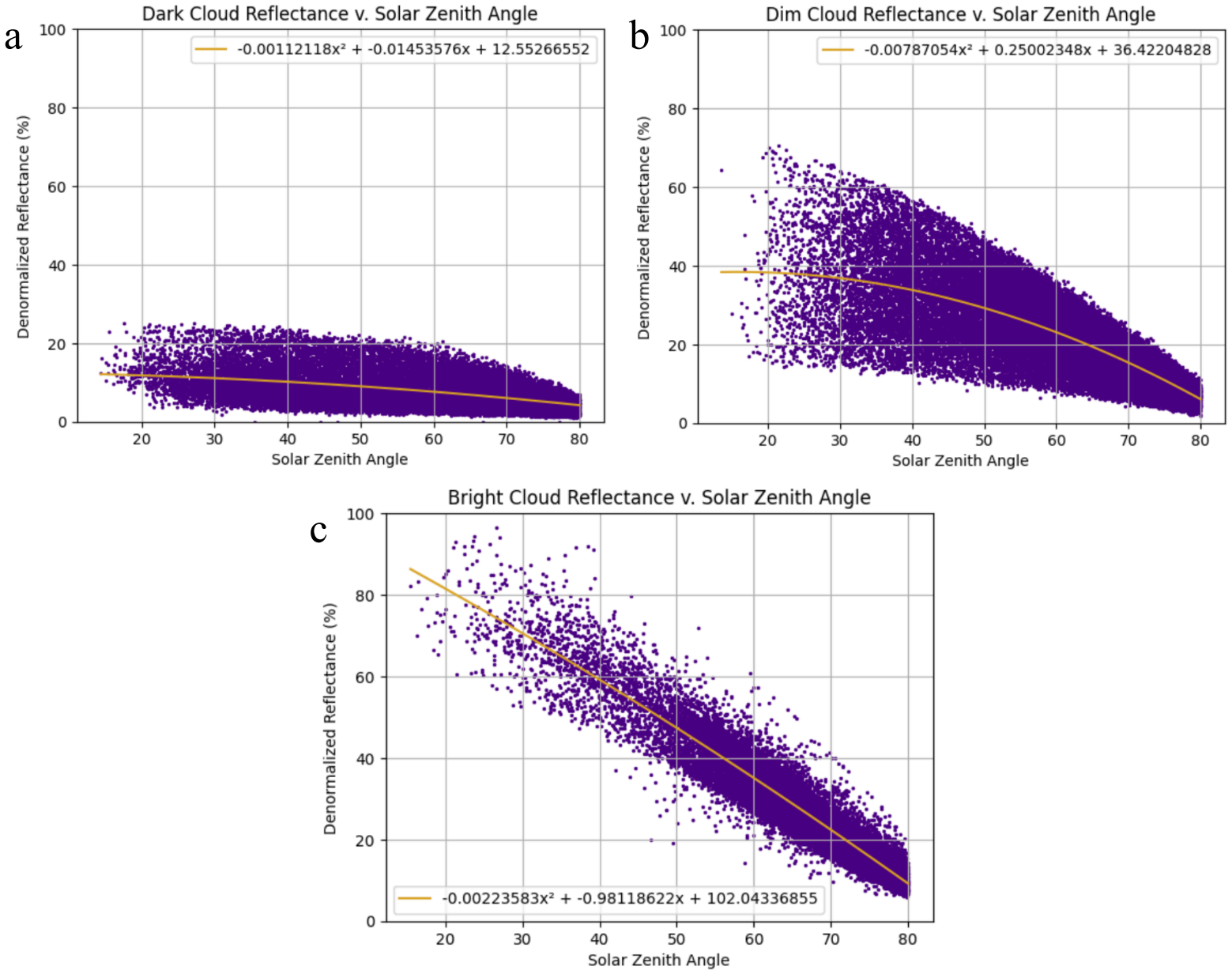

Figure 3.3: Reflectance-SZA scatterplots for (a) dark clouds, (b) dim clouds, and (c) bright clouds, complete with 2nd-degree polynomial fit lines. Reflectance is de-normalized to eliminate the original μ-normalization applied to the PATMOS-x 0.65-μm reflectance variable.

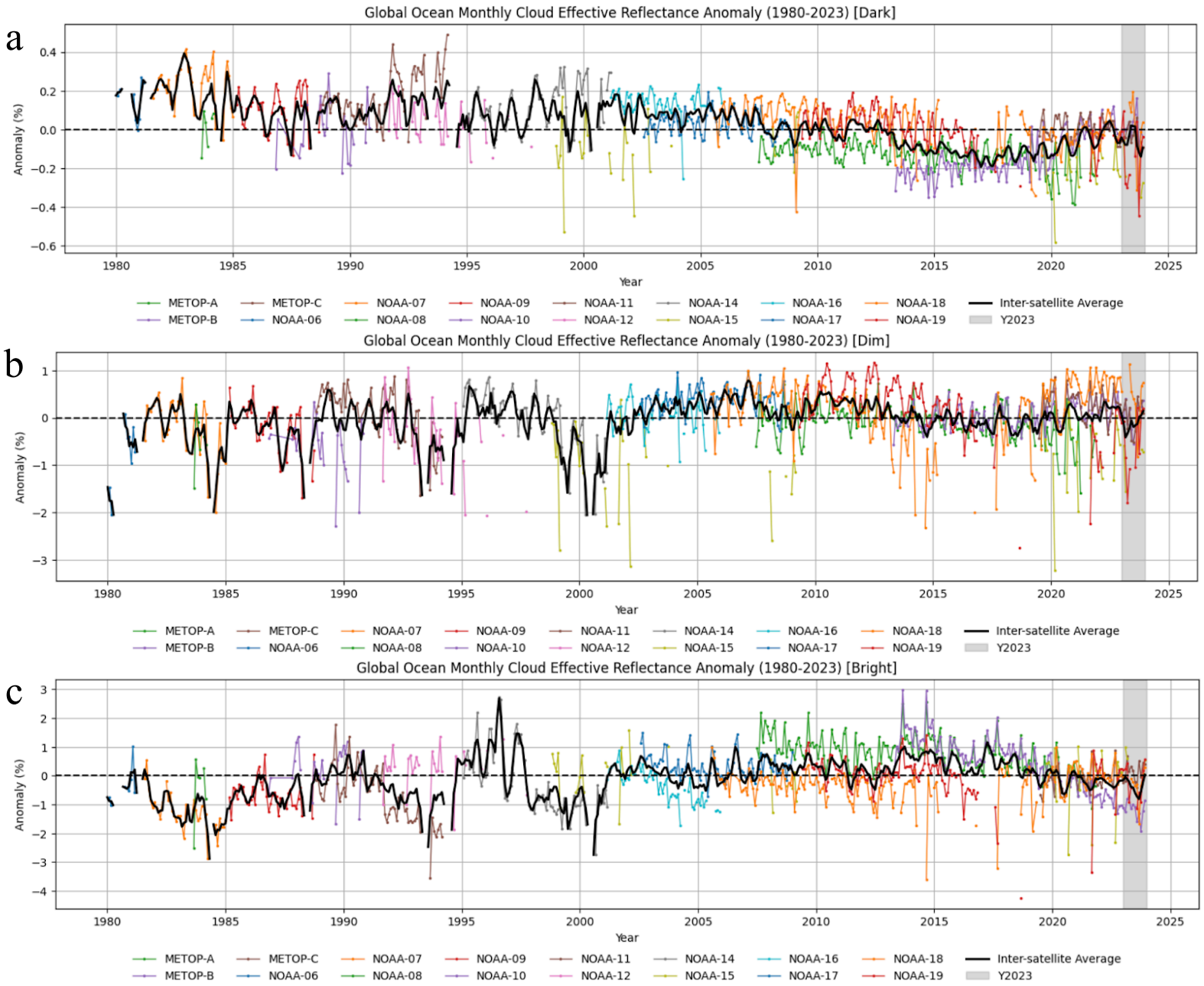

Figure 3.4: Global, oceans-only monthly mean CER anomaly time series, parsed by satellite, normalized, and deseasonalized for (a) dark clouds, (b) dim clouds, and (c) bright clouds from 1980 to 2023. Gray bars highlight the months of 2023, and the black line quantifies the average inter-satellite CER anomaly.

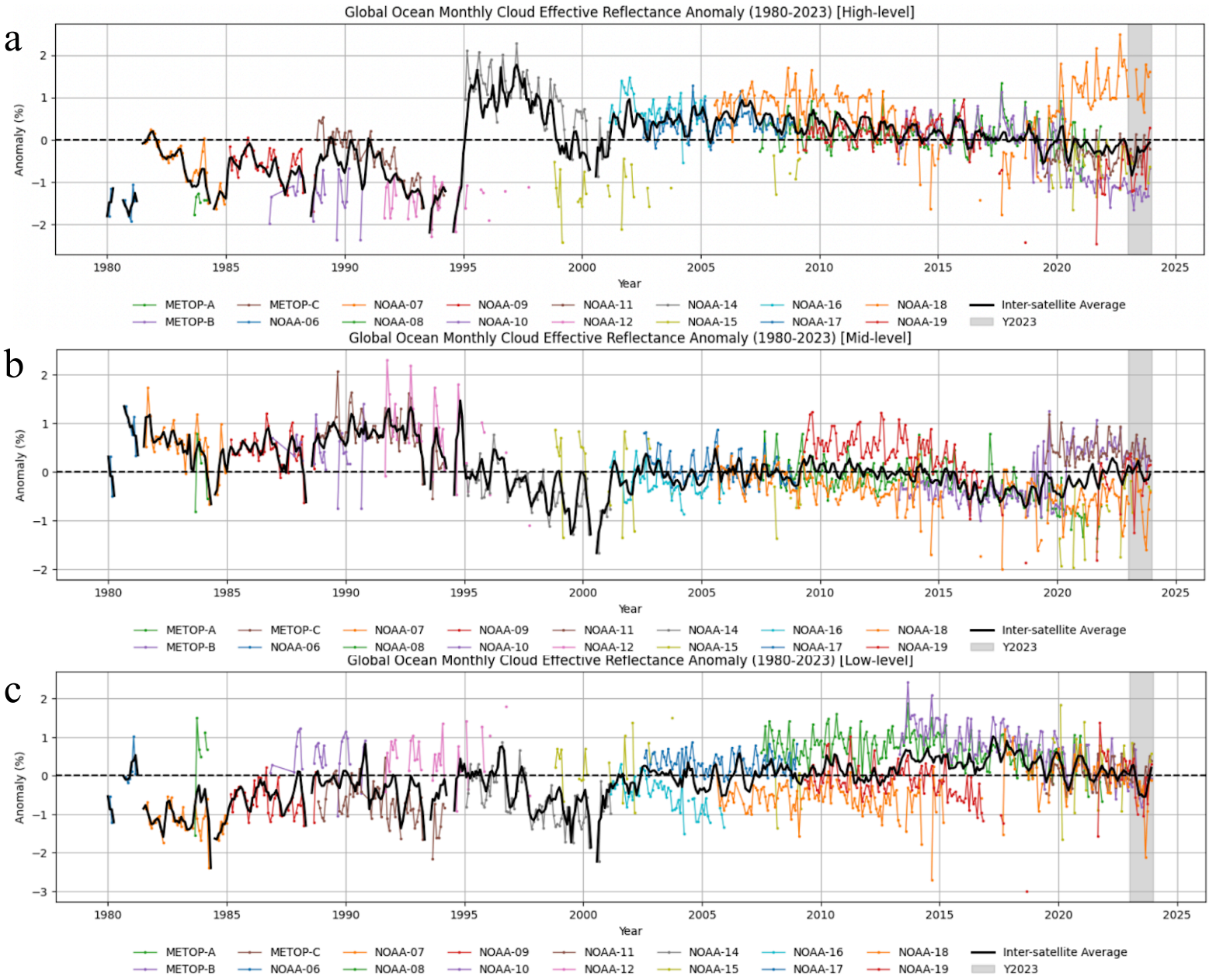

Figure 3.5: Global, oceans-only monthly mean CER anomaly time series, parsed by satellite, normalized, and deseasonalized for (a) upper-level clouds, (b) mid-level clouds, and (c) low-level clouds from 1980 to 2023. Gray bars highlight the months of 2023, and the black line quantifies the average inter-satellite CER anomaly.

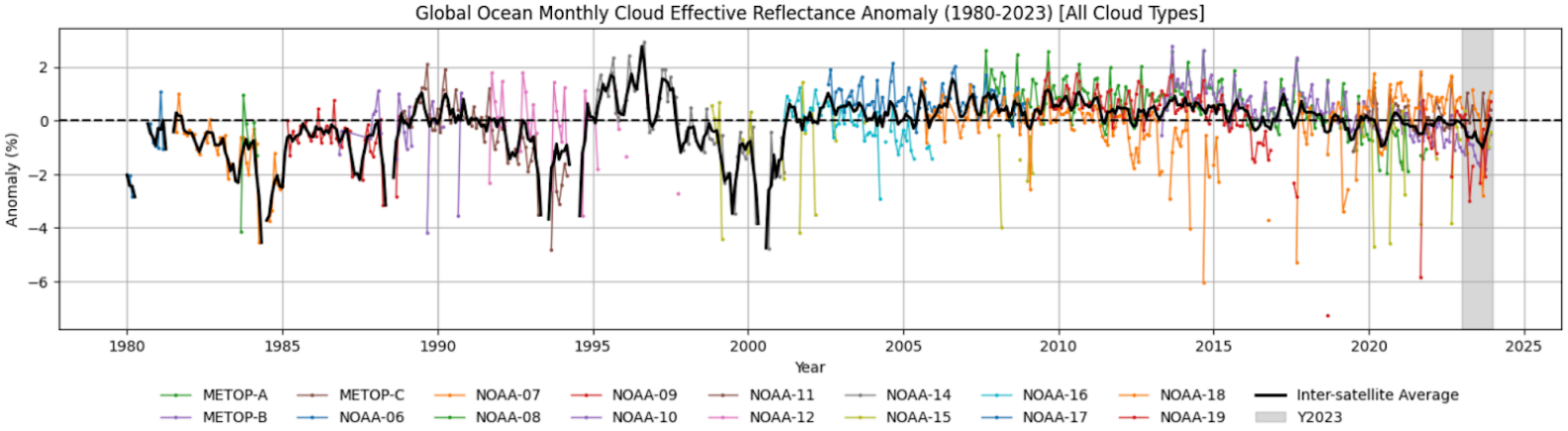

Figure 3.6: Global, oceans-only monthly mean CER anomaly time series, parsed by satellite, normalized, and deseasonalized for all clouds from 1980 to 2023. Gray bars highlight the months of 2023, and the black line quantifies the average inter-satellite CER anomaly.

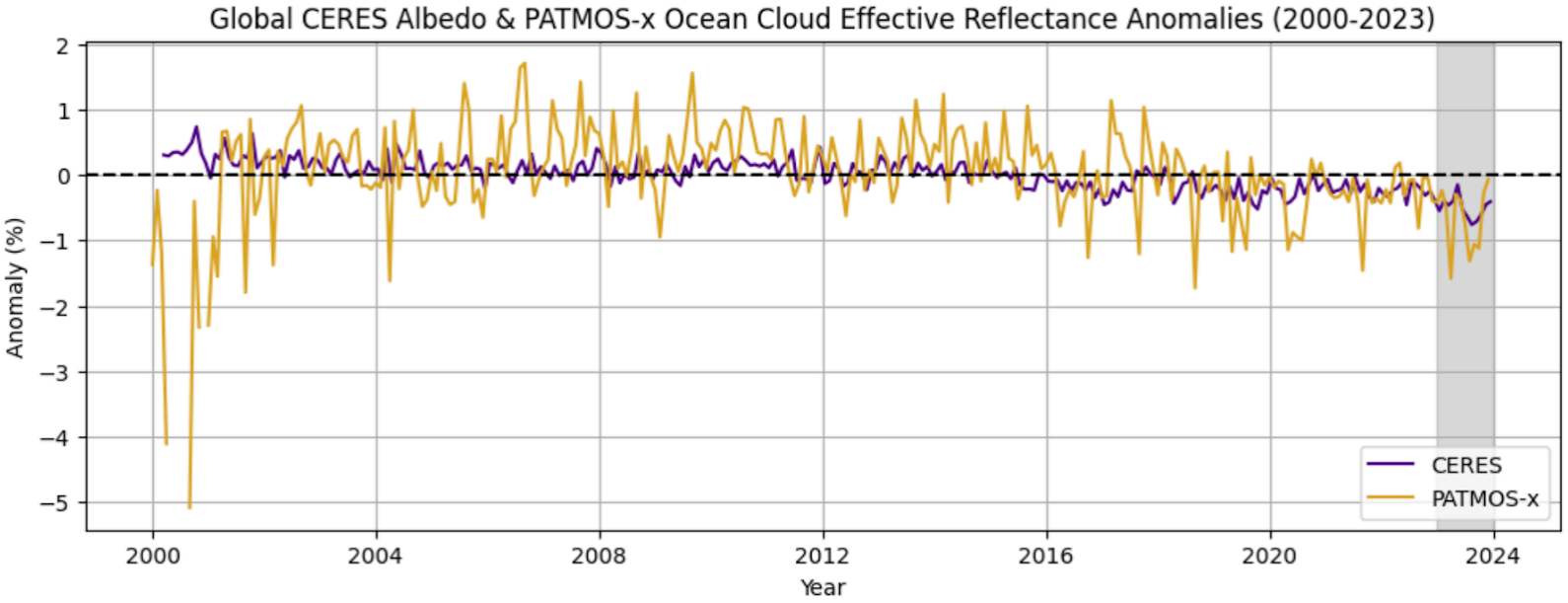

Figure 3.7: Anomaly time series comparison of PATMOS-x global, all-cloud, oceans-only CER inter-satellite average and CERES-EBAF global, all-sky planetary albedo from 2000 to 2023. The gray bar highlights the months of 2023.

3.3. Central Indian Ocean Case Study

While conducting a global analysis of CER has proven to be complex and uncertain at best, the scope of analysis can be narrowed back down to a specific ocean region to assess the performance of PATMOS-x in a more local context. In this section, the focus area is centered on the Central Indian Ocean (CIO): λ = (50º E, 120º E) and ϕ = (30º S, 10º N). Figure 3.8 shows consistent, strong anomaly signals in this region for (a) planetary albedo (negative), (b) absorbed solar radiation (positive), (c) TOA outgoing longwave flux (positive), and (d) total cloud CER (negative) in 2023, implying a high likelihood that, for that year, there was a significant decrease in cloud cover.

3.3.1. PATMOS-x Time Series Analysis

CER anomaly for all cloud types from 1980 to 2023 over the CIO is shown in Figure 3.9, wherein some of the same disagreements between early satellites that were previously observed in Figure 3.6 are present; however, there is marked improvement in the later satellites' agreement and no significant drift signal past 2000. Breaking CER anomaly down to its three COD bins (Figure 3.10) yields a relatively stable, slight downtrend in dark CER anomaly (Figure 3.10a) throughout the record; NOAA-06 is in no agreement with any other satellite, and there is a faint discontinuity between NOAA-14 and NOAA-16, but post-2000, the record demonstrates reasonable inter-satellite agreement. Dim CER anomaly (Figure 3.10b) reveals only one pronounced discontinuity between NOAA-14 and NOAA-15 and a negative outlier in 1995; otherwise, the record is largely stable and presents good inter-satellite agreement. Bright CER anomaly (Figure 3.10c) is the apparent source of the early satellite disagreements in Figure 3.9, exhibiting the same pattern of consistently higher-recorded measurements in NOAA-08, -10, -12,

and -15, all of which are morning-orbit platforms; they all fly with similar LOTs. Post-2000, there is a slight disagreement between the METOPs and NOAA satellites, especially from 2007 to 2017, with the METOPs recording higher CER than the NOAA platforms. However, this disagreement is small – on the order of <1%.

If the perspective is shifted to analyze CER by level (Figure 3.11), high-level clouds (Figure 3.11a) exhibit the most stable and reliable behavior, with solid inter-satellite agreement throughout the entire record with the exception of NOAA-06. This is consistent with the fact that upper-level clouds are always the first targets a satellite observes, meaning there are fewer geometric uncertainties stemming from the potential of overlapping and obscuration by other clouds as well as influences from atmospheric scattering. Mid-level clouds (Figure 3.11b) show disagreement among early satellites, but post-2000, measurements from all satellites align well with one another. Low-level clouds (Figure 3.11c) also show the same early satellite disagreement presented by bright clouds (Figure 3.10c) and the total cloud CER time series (Figure 3.9), which ultimately suggests that it is specifically the low-bright clouds that are the dominant contributors to inter-satellite disagreements pre-2000 over the CIO.

The stark improvement in inter-satellite agreement and measurement stability on a per-platform basis upon narrowing the scope of analysis down to a small oceanic region is indicative of the tendency of the SZA normalization methodology to handle orbital drift and LOT discontinuities much more adequately when not applied and averaged globally. Overall, though these discrepancies are not entirely resolved by regional analysis as opposed to global analysis, PATMOS-x performs reasonably well as a means for CER investigations under the condition that analysis is confined to a relatively localized oceanic domain.

3.3.2. Comparison of PATMOS-x to CERES-EBAF

An inter-satellite average of PATMOS-x all-cloud CER anomaly comparison to CERES-EBAF planetary albedo anomaly from 2000 to 2023 is shown by Figure 3.12a. Here, the agreement between PATMOS-x and CERES is much improved from the global analysis comparison (Figure 3.7); the magnitudes of local maxima and minima align frequently. As well, Figure 3.13 shows a strong correlation between CERES albedo anomaly and PATMOS-x CER anomaly, with an R^2 value of ~0.7227. Unlike the global mean planetary albedo (Figure 1.1), the CIO mean albedo anomaly does not feature a steady decline over time, nor does CER anomaly. However, most notably, in the months of 2023 (Figure 3.12b), both PATMOS-x CER anomaly and CERES planetary albedo anomaly exhibit near-congruent behavior, effectively supporting the hypothesis that clouds were not only dominant contributors to the region's strong negative albedo anomaly that year, but likely the sole contributors. This is the expected outcome over a tropical ocean – as there are no other bright, highly-variable targets in such a domain – and lends credence to the ability of PATMOS-x to accurately capture reflective patterns and characteristics of clouds post-2000.

The analysis can be deepened from here; to determine which specific cloud types or bins are responsible for the strong radiative anomaly signals over the CIO in Figure 3.8, CER anomaly time series are repeated over the 2000-2023 timeframe and spatial maps are generated for each COD bin (Figure 3.14) and level bin (Figure 3.15). Dark CER anomaly (Figure 3.14a) shows an apparent downtrend over time and a consistent negative anomaly for the entirety of 2023; however, spatial analysis for that year (Figure 3.14d) shows that this constant negative anomaly barely registers over the CIO – or anywhere in the world. This is a clear feature of dark clouds as optically thin, poor reflectors; a downtrend or consistent below-average anomaly in cloud fraction – factored

into the CER computation – does not necessarily result in a significant impact on the effective reflectance. Dim clouds (Figure 3.14b) exhibit no trend over time; however, there is a dip in CER anomaly in 2023, and CER remains below the climatological average for nearly the entire year. The associated CER anomaly map (Figure 3.14e) reveals a relatively pronounced negative anomaly over the Indian Ocean. Bright clouds (Figure 3.14c) evince a slight *uptrend* in CER over time. Although, in 2023, these clouds also show a negative anomaly for the entire year, only not as prominently as the dim clouds, ultimately translating to a faded and not especially remarkable negative anomaly centered over the Indian Ocean on the map (Figure 3.14f).

Evidently, it is not any one COD bin of clouds that appears to contribute most dominantly to the strong 2023 anomaly signal observed by both CERES and PATMOS-x. Overwhelmingly, the cause of the 2023 CER and albedo anomalies over the CIO is rooted, instead, in the level bins, shown in Figure 3.15. In fact, the map of upper-level cloud CER anomaly (Figure 3.15d) shows nearly an exact match for the CERES planetary albedo, absorbed solar radiation, and TOA longwave flux anomalies over the Indian Ocean, in both spatial appearance and relative magnitude. The associated time series (Figure 3.15a), unsurprisingly, reveals that the CER for these clouds is below-average for all months of 2023. On the other hand, time series of mid-level (Figure 3.15b) and low-level (Figure 3.15c) clouds show comparatively nominal anomalies over the CIO, and their associated maps – Figure 3.15e and Figure 3.15f, respectively – confirm that their contribution to the 2023 CIO albedo anomaly is almost entirely insignificant. Thus, if it is dim clouds that are the dominant contributors from the perspective of COD bin, and it is upper-level clouds that are the dominant contributors from the perspective of level bin, it can be reasonably concluded that it is specifically high-dim clouds that were the primary drivers of 2023's negative albedo anomaly over the CIO. This is supported by CER anomaly time series and maps generated

for high-dark (Figure 3.16a and 3.16d), high-dim (Figure 3.16b and 3.16e), and high-bright (Figure 3.16c and 3.16f) clouds. High-dim clouds show the greatest-magnitude negative anomalies for the months of 2023 (Figure 3.16b) and the most pronounced spatially-represented negative anomaly signal over the Indian Ocean (Figure 3.16e).

Figure 3.17a compares inter-satellite averages of PATMOS-x all-cloud CER anomaly and upper-level CER anomaly to CERES albedo anomaly over the CIO for the months of 2023, showing that all three quantities tend to follow the same patterns of behavior and variability throughout the year; the only instances in which the upper-level CER anomaly notably deviates from all-cloud CER anomaly and albedo anomaly, there is a coincident local maximum or minimum in low-level CER anomaly that offsets the impact of upper-level CER anomaly, as demonstrated in Figure 3.17b. Mid-level CER exhibits no significant impact.

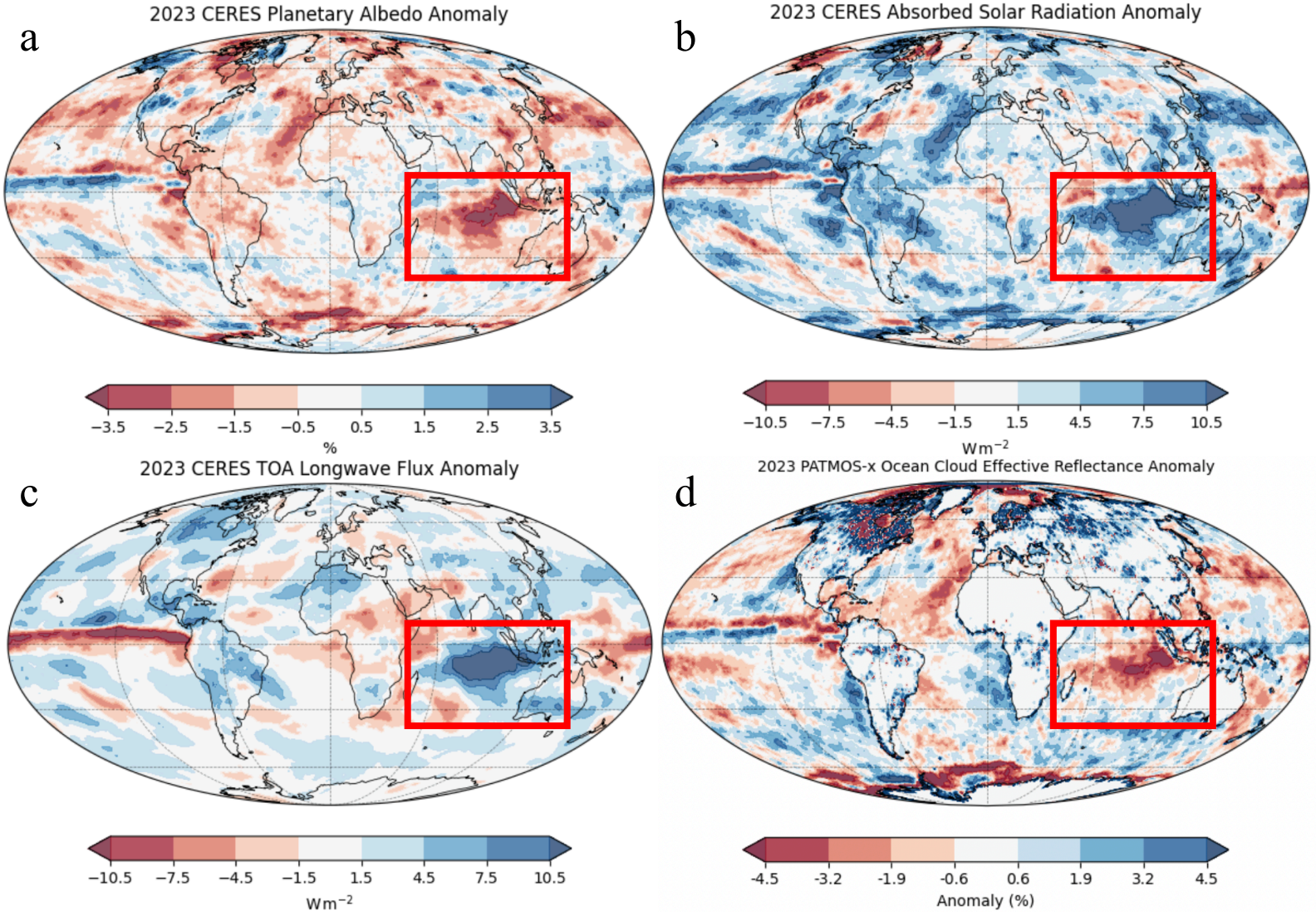

Figure 3.8: Spatial maps of (a) CERES-EBAF planetary albedo anomaly, (b) CERES-EBAF absorbed solar radiation anomaly, (c) CERES-EBAF top-of-atmosphere longwave flux anomaly, and (d) PATMOS-x ocean CER anomaly. Red boxes indicate case study region: Central Indian Ocean.

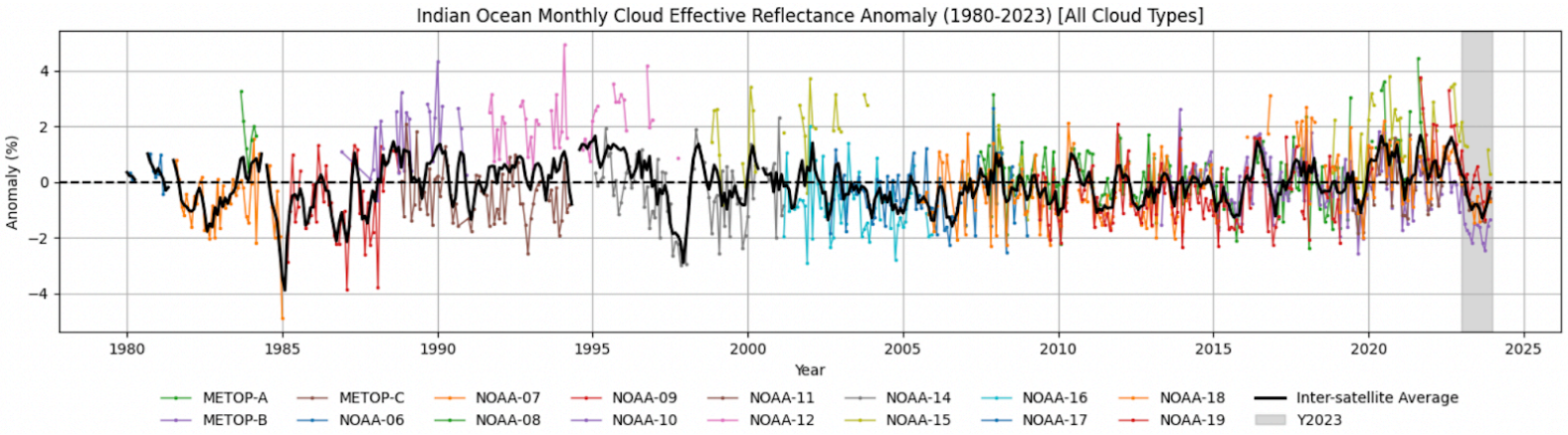

Figure 3.9: Central Indian Ocean monthly mean CER anomaly time series, parsed by satellite, normalized, and deseasonalized for all clouds from 1980 to 2023. Gray bars highlight the months of 2023, and the black line quantifies the average inter-satellite CER anomaly.

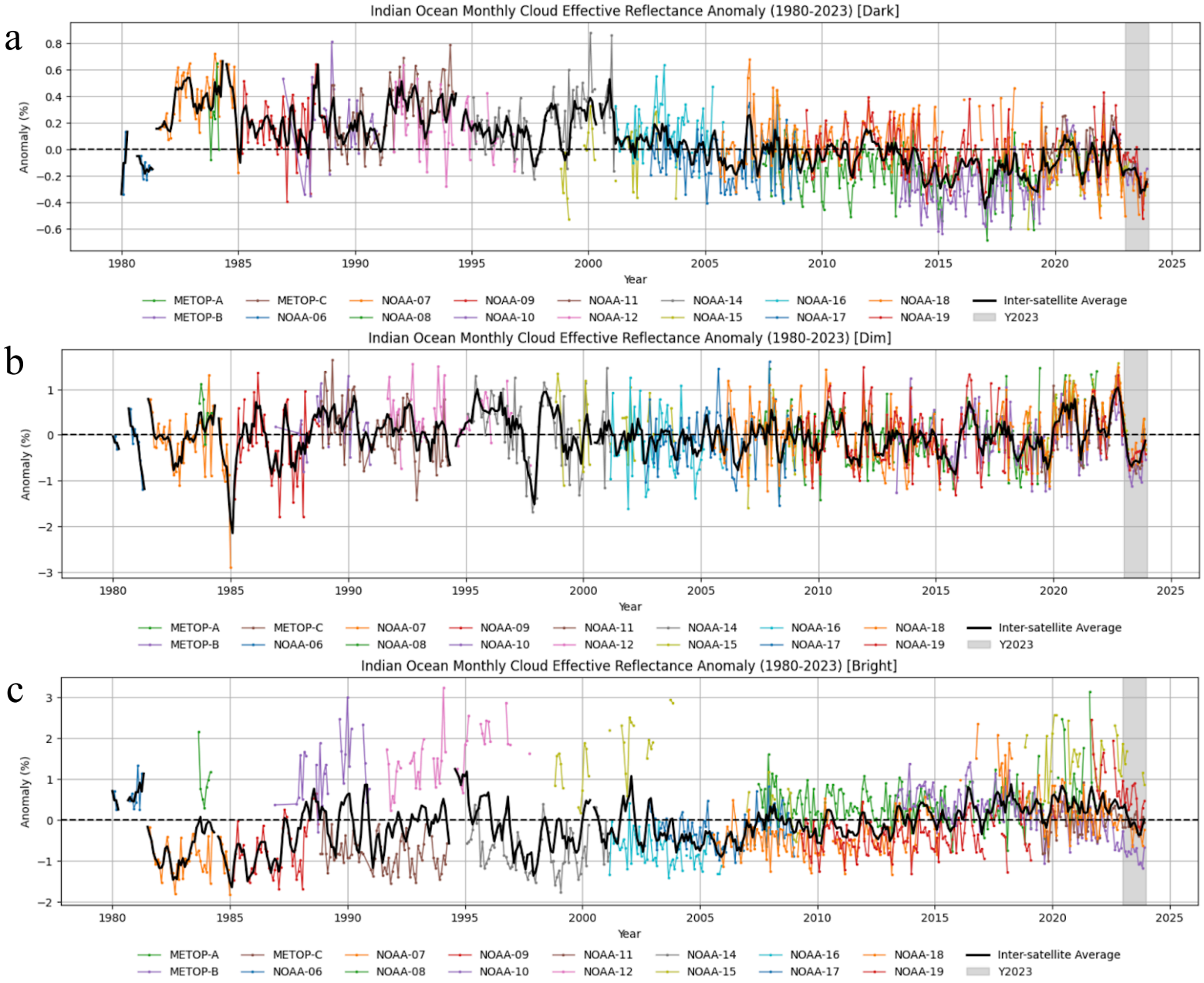

Figure 3.10: Central Indian Ocean monthly mean CER anomaly time series, parsed by satellite, normalized, and deseasonalized for (a) dark clouds, (b) dim clouds, and (c) bright clouds from 1980 to 2023. Gray bars highlight the months of 2023, and the black line quantifies the average inter-satellite CER anomaly.

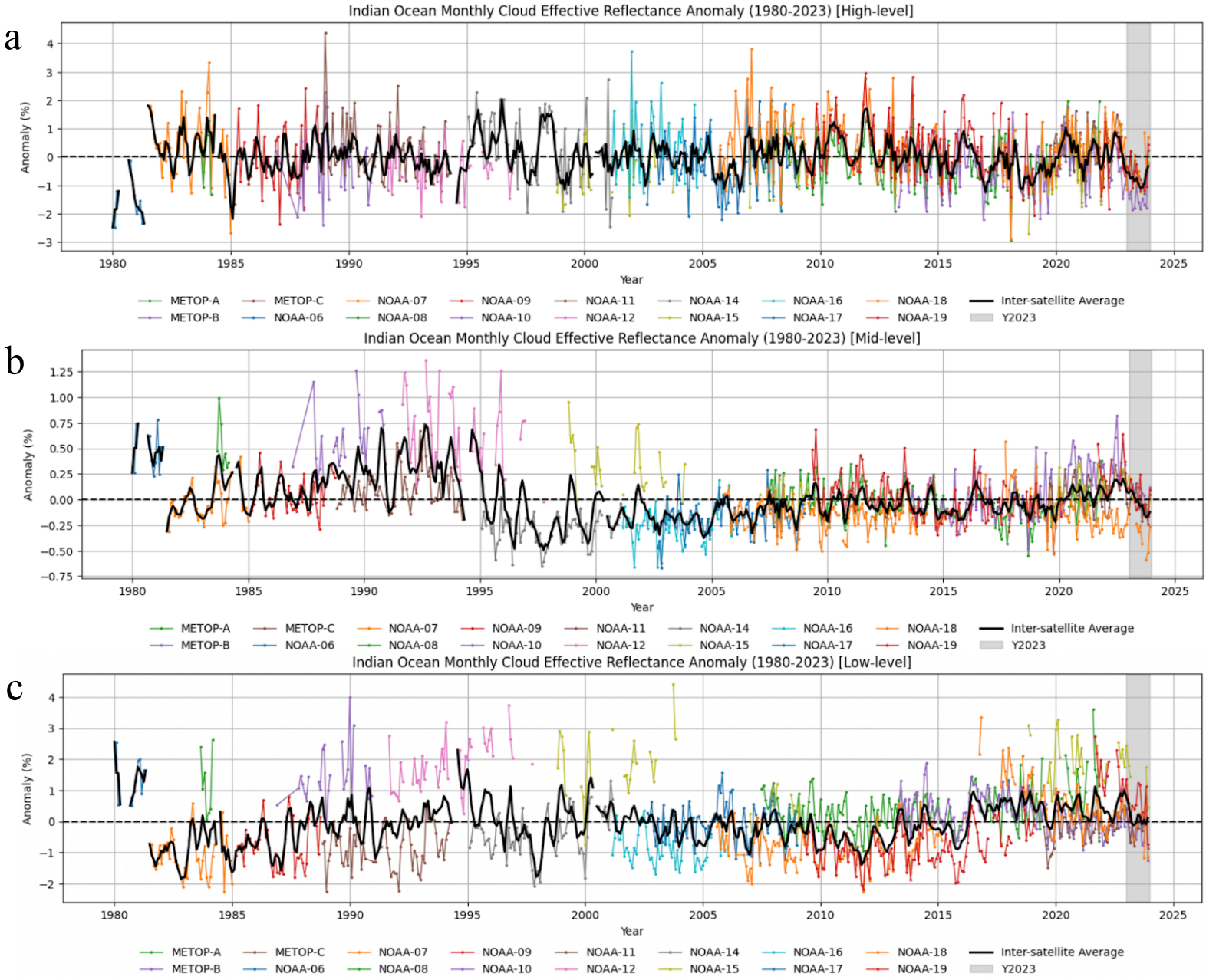

Figure 3.11: Central Indian Ocean monthly mean CER anomaly time series, parsed by satellite, normalized, and deseasonalized for (a) upper-level clouds, (b) mid-level clouds, and (c) low-level clouds from 1980 to 2023. Gray bars highlight the months of 2023, and the black line quantifies the average inter-satellite CER anomaly.

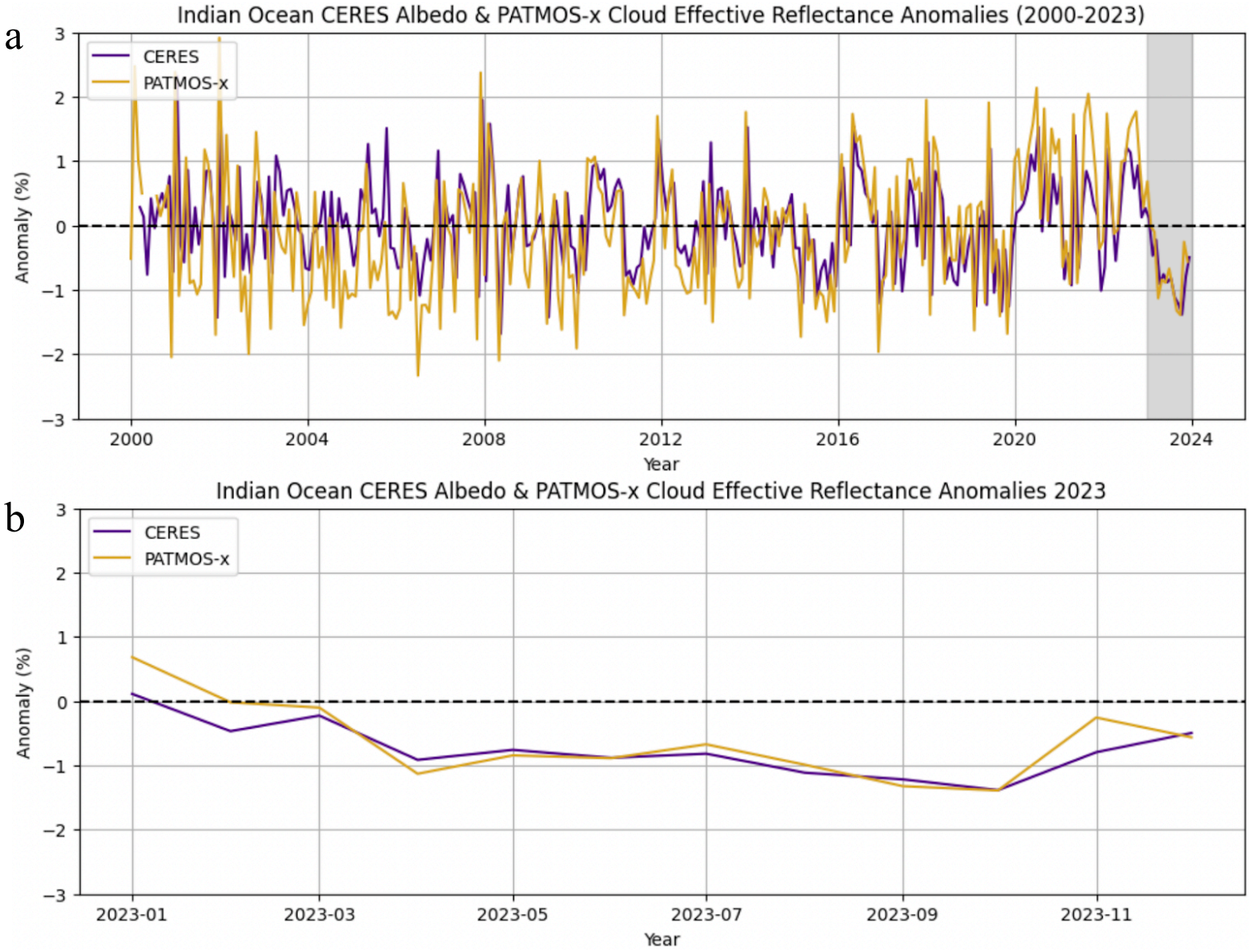

Figure 3.12: Anomaly time series comparison of PATMOS-x all-cloud CER inter-satellite average and CERES-EBAF all-sky planetary albedo over the Central Indian Ocean (a) from 2000 to 2023 and (b) for the months of 2023. The gray bar in (a) highlights the months of 2023.

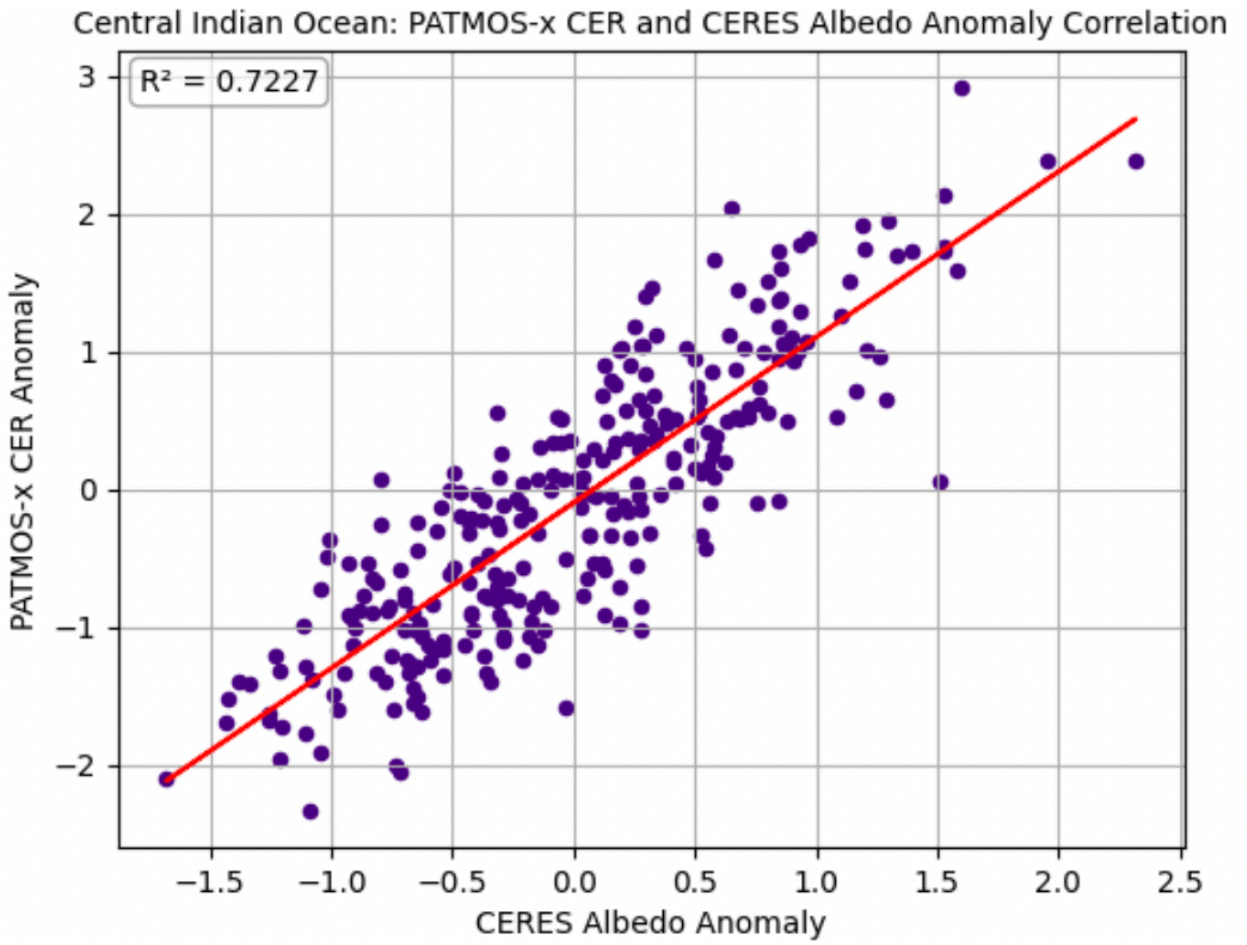

Figure 3.13: Linear regression correlation between CERES planetary albedo anomaly and PATMOS-x CER anomaly over the Central Indian Ocean from 2000 to 2023. R^2 value is 0.7227.

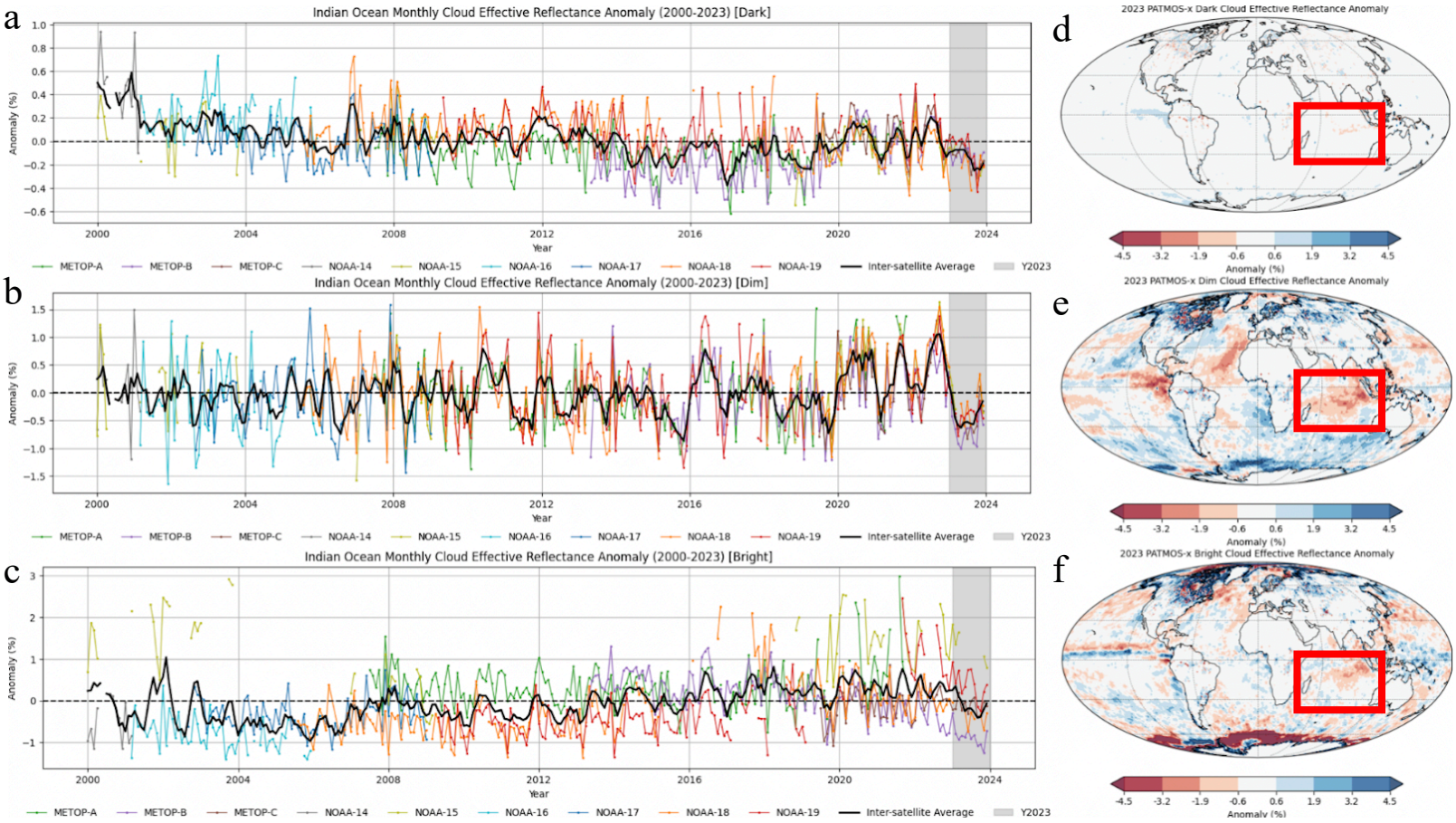

Figure 3.14: Central Indian Ocean monthly mean CER anomaly time series, parsed by satellite, normalized, and deseasonalized for (a) dark clouds, (b) dim clouds, and (c) bright clouds from 2000 to 2023, and 2023 spatial maps of CER anomaly for (d) dark clouds, (e) dim clouds, and (f) bright clouds. Gray bars highlight the months of 2023, and the black line quantifies the average inter-satellite CER anomaly.

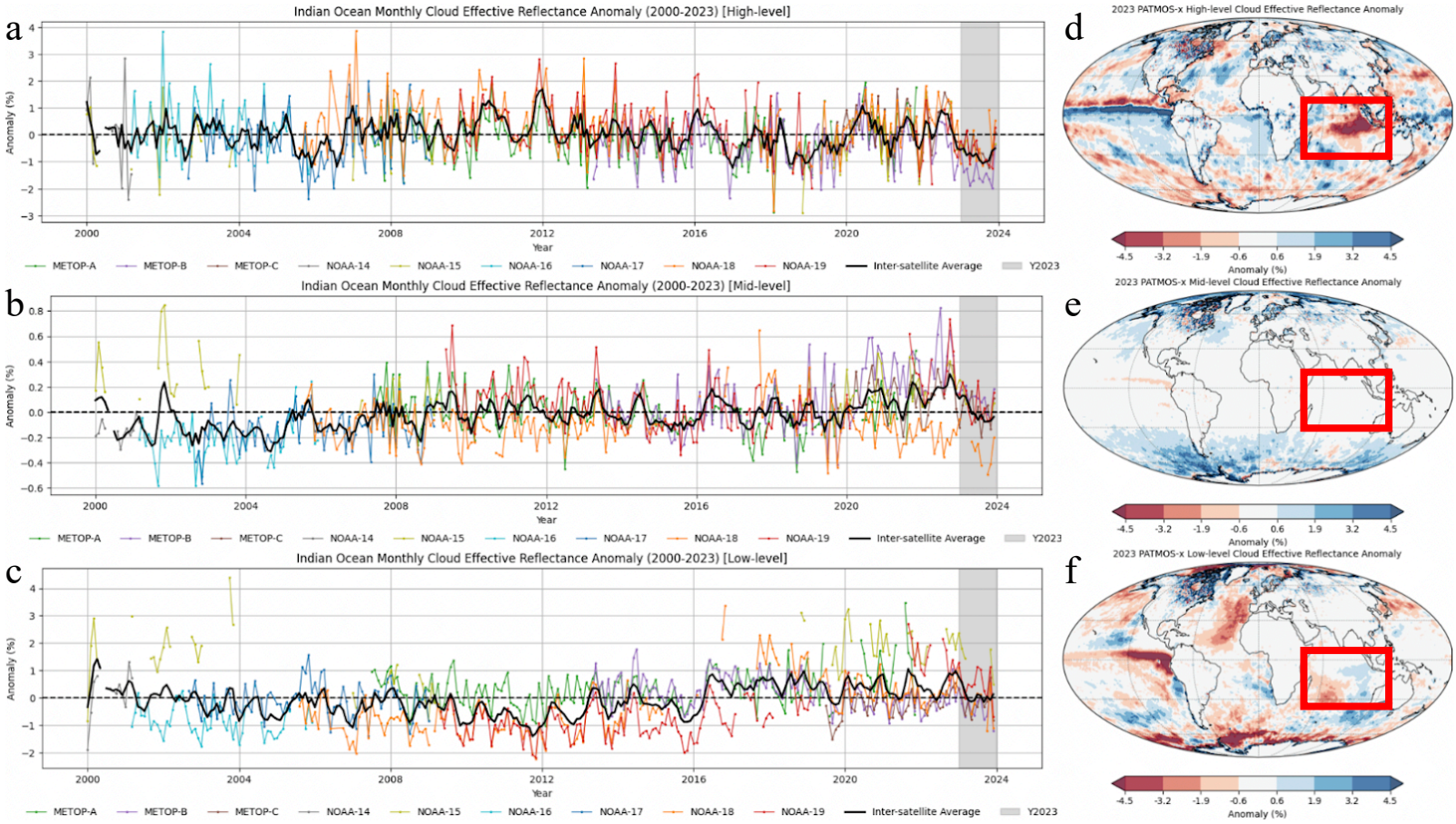

Figure 3.15: Central Indian Ocean monthly mean CER anomaly time series, parsed by satellite, normalized, and deseasonalized for (a) upper-level clouds, (b) mid-level clouds, and (c) low-level clouds from 2000 to 2023, and 2023 spatial maps of CER anomaly for (d) upper-level clouds, (e) mid-level clouds, and (f) low-level clouds. Gray bars highlight the months of 2023, and the black line quantifies the average inter-satellite CER anomaly.

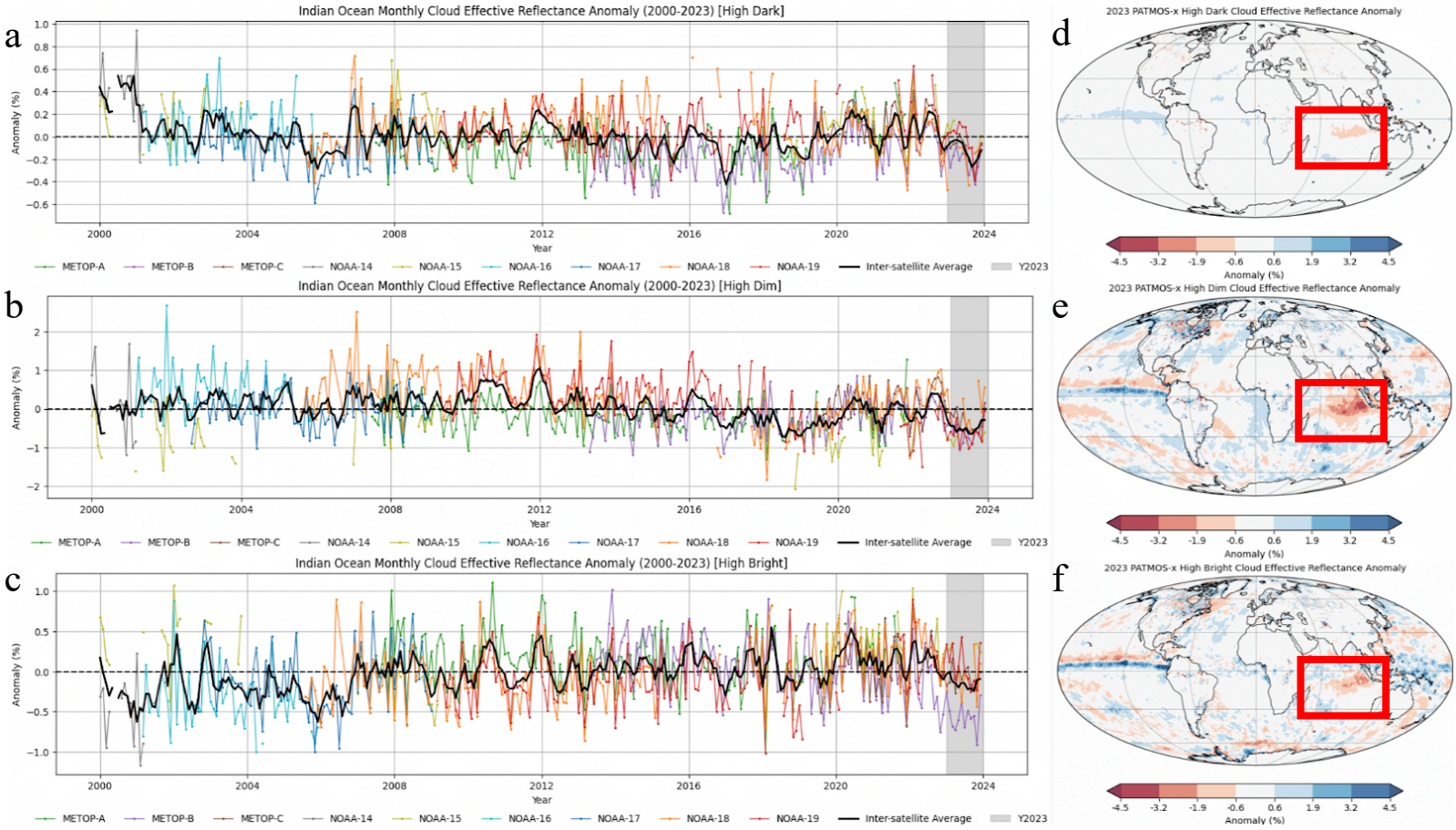

Figure 3.16: Central Indian Ocean monthly mean CER anomaly time series, parsed by satellite, normalized, and deseasonalized for (a) high-dark clouds, (b) high-dim clouds, and (c) high-bright clouds from 2000 to 2023, and 2023 spatial maps of CER anomaly for (d) high-dark clouds, (e) high-dim clouds, and (f) high-bright clouds. Gray bars highlight the months of 2023, and the black line quantifies the average inter-satellite CER anomaly.

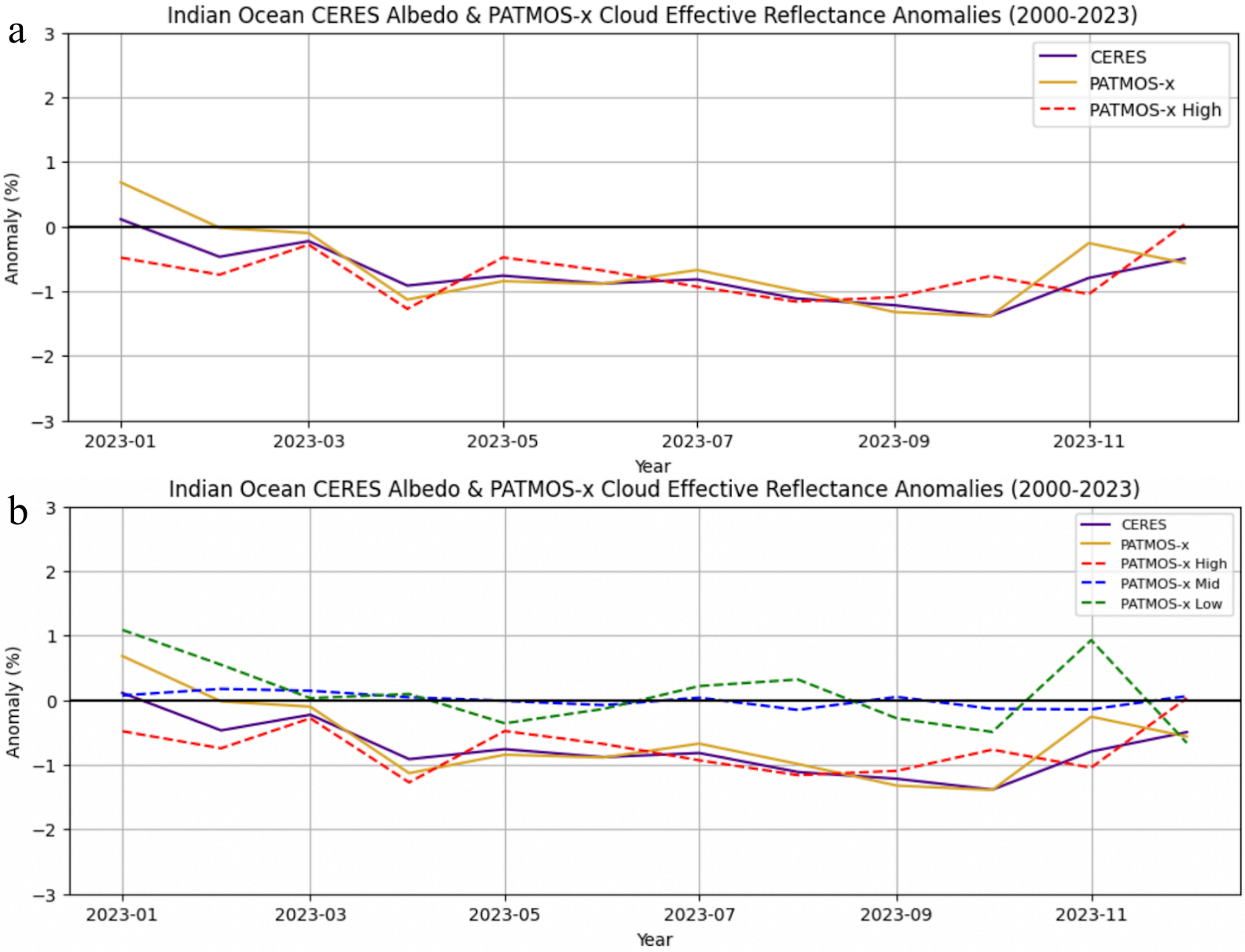

Figure 3.17: Anomaly time series comparison of (a) PATMOS-x all-cloud CER inter-satellite average, PATMOS-x upper-level CER inter-satellite average, and CERES-EBAF all-sky planetary albedo and (b) PATMOS-x all-cloud CER inter-satellite average, PATMOS-x upper-level CER inter-satellite average, mid-level CER inter-satellite average, low-level CER inter-satellite average, and CERES-EBAF all-sky planetary albedo over the Central Indian Ocean for the months of 2023.

Chapter 4

Discussion and Future Work

4.1. Summary

From 2000 to 2023, there was a notable decline in global, all-sky planetary albedo, with a record low occurring mid-year in 2023, as determined by the CERES-EBAF climate record. Clouds were posited as the most likely contributors to this decline and record low; however, due to the limitations presented by the CERES-EBAF data availability of cloud properties and products, in-depth analysis of the role of clouds could not be conducted with the CERES-EBAF record. 0.65-μm visible reflectance sourced from the PATMOS-x cloud CDR was the proposed alternative to serve the purpose of analyzing how reflective changes in clouds may have driven similar albedo changes globally. Its implementation of data from AVHRR-based satellite platforms presented challenges on the basis of the AVHRR sensor's intended use being for operational environmental observation rather than climate monitoring. The lack of onboard calibration for AVHRR, compilation of data from satellites flying with different LOTs, and the tendency of NOAA's polar-orbiting platforms to drift out of their original orbit necessitated a

validation of the PATMOS-x inter-sensor calibration and a revision of the SZA normalization pre-applied to the record's 0.65-μm reflectance variable.

The validation exercise involved the use of tropical DCCs as stable targets to evaluate the stability of visible reflectance across the record. With the derivation and application of a novel reflectance-SZA relationship to eliminate SZA-based inter-satellite discontinuity phenomena, the PATMOS-x intercalibration demonstrated adequate resolution of time-dependent sensor degradation and its impacts on data retrievals. The desired maximum uncertainty range of monthly mean stable target reflectance was 4%, and the vast majority of the tropical DCC points fell within this range, establishing the PATMOS-x Level-2bc record as a reasonable candidate for the successive investigations of global and regional cloud effective reflectance.

Ultimately, however, it was determined that, while the intercalibration for PATMOS-x is sound, opening the scope of reflectance analysis to all cloud types on a global scale introduces complications the SZA normalization methodology developed in the validation phase cannot sufficiently resolve. Clouds falling into the thinnest COD bin posed issues with reflectance retrievals over snow, ice, and deserts, prompting the application of a filter to remove samples taken over land, inland water sources, and ephemeral water sources. Even with this adjustment, orbital drift and disagreements, particularly in the pre-2000 satellites, remained a significant factor of degradation to measurement accuracy in all global ocean-only analysis time series from 1980 to 2023. No trends in CER could be confidently gleaned, and the application of the oceans-only filter rendered comparison of the all-cloud inter-satellite CER average against the CERES-EBAF all-sky planetary albedo somewhat ineffectual.

In a CER case study over the Central Indian Ocean, however, there was marked improvement in the degree to which the SZA normalization resolved orbital drift and

discontinuities across all satellite platforms. Upper-level clouds presented near-congruent reflective anomaly behavior to that of CERES albedo in 2023, and it was concluded that high-dim clouds – falling within the <410-mb CTP range, 3.6-23 COD range, and 30-45% mean reflectance range – were the driving force behind the pronounced negative albedo anomaly in the CIO region. This finding is well-supported by the agreement observed between PATMOS-x inter-satellite all-cloud CER anomaly, upper-level CER anomaly, and CERES all-sky albedo anomaly.

It is therefore determined that PATMOS-x is not, in its current form, a reliable dataset for full, global time series analyses of 0.65-μm cloud reflectance and related quantities, as the SZA normalization method developed to handle inter-satellite disagreements does not perform adequately in the case of thin clouds above bright surfaces, or when reflectance averages are taken across the full domain of latitudes and longitudes. Alternatively, PATMOS-x performs quite reliably when the scope of analysis is narrowed down to relatively small oceanic regions.

4.2. Future Work

The fact that the SZA normalization method does not behave as desired in global, ocean-based analyses raises the important question of: why? Ideally, the application of an oceans-only filter, as previously described, should have allowed the SZA normalization to resolve orbital drift and inter-satellite disagreements much more effectively than it could when analysis was attempted without an oceans-only filter. Returning to Figure 3.8d reveals that it is not necessarily the SZA normalization method that is faulty, but rather, the oceans-only filter. The map of 2023 PATMOS-x all-cloud CER anomaly shows that outlier CER data points are still being recorded over landmasses and inland water sources; this means that the strong positive anomalies and strong negative anomalies populating these regions were factored into the global, oceans-only CER

monthly mean calculation for time series analysis, suggesting a potential need to revise the land mask categories supplied in the PATMOS-x record. Furthermore, due to the presence of strong anomalies recorded near the poles, the introduction of a snow and sea-ice filter may be beneficial, as these anomalies are more likely to be sea-ice-related than they are to be true cloud-related reflective anomalies. With these changes, the performance of the SZA normalization method developed in this thesis should improve substantially, decreasing the number of sources of uncertainty that made global analysis over oceans unproductive.

However, to ensure the reliability of PATMOS-x in a *complete* global analysis, the issue of anomalously high reflectance being incorrectly attributed to optically thin clouds present over bright surfaces must be addressed. What prompted the need for an oceans-only filter to begin with was the frequent inability of AVHRR sensors to distinguish between the reflectance of an optically thin cloud and the reflectance of the surface underneath it. Evidently, while the record can correctly identify that a thin cloud is present, it cannot always properly return a reflectance within the expected physical range. Revisiting this issue would likely begin with amending the assumption that all targets viewed by the sensor are functionally opaque and potentially continue with the development of a corrective algorithm that can return physically appropriate reflectance values in cases of optically thin cloud formation over ice sheets, snow, and deserts. Doing so would effectively serve to improve the reliability of PATMOS-x in full global analyses pertaining to cloud reflectance.

References

Ackerman, S.A. and Coauthors, 2019: Satellites See the World's Atmosphere, https://doi.org/10.1175/AMSMONOGRAPHS-D-18-0009.1.

Bacour, C., F.M. Bréon, L. Gonzalez, I. Price, J.P. Muller, and A.G. Straume, 2020: Simulating Multi-Directional Narrowband Reflectance of the Earth's Surface Using ADAM (A Surface Reflectance Database for ESA's Earth Observation Missions). *Remote Sensing*, **12**, 1679, https://doi.org/10.3390/rs12101679.

Bender, F.A.M., A. Engström, and J. Karlsson, 2016: Factors Controlling Cloud Albedo in Marine Subtropical Stratocumulus Regions in Climate Models and Satellite Observations, https://doi.org/10.1175/JCLI-D-15-0095.1.

Bhatt, R., D.R. Doelling, B.R. Scarino, A. Gopalan, C.O. Haney, P. Minnis, and K.M. Bedka, 2016: A Consistent AVHRR Visible Calibration Record Based on Multiple Methods Applicable for the NOAA Degrading Orbits. Part I: Methodology, https://doi.org/10.1175/JTECH-D-16-0044.1.

Bojanowski, J.S., and J.P. Musiał, 2020: Dissecting effects of orbital drift of polar-orbiting satellites on accuracy and trends of climate data records of cloud fractional cover. *Atmospheric Measurement Techniques*, **13**, 6771–6788, https://doi.org/10.5194/amt-13-6771-2020.

Chen, Y.C., M.W. Christensen, G.L. Stephens, and J.H. Seinfeld, 2014: Satellite-based estimate of global aerosol–cloud radiative forcing by marine warm clouds. *Nature Geosci*, **7**, 643–646, https://doi.org/10.1038/ngeo2214.

Doelling, D. R., L. Nguyen, and P. Minnis, 2004: On the use of deep convective clouds to calibrate AVHRR data. W.L. Barnes and J.J. Butler, Eds, Optical Science and Technology, the SPIE 49th Annual Meeting, Denver, CO, 281, https://doi.org/10.1117/12.560047.

Duspayev, A., M.G. Flanner, and A. Riihelä, 2024: Earth's Sea Ice Radiative Effect From 1980 to 2023. *Geophysical Research Letters*, **51**, e2024GL109608, https://doi.org/10.1029/2024GL109608.

Foster, M. J., and A. Heidinger, 2013: PATMOS-x: Results from a Diurnally Corrected 30-yr Satellite Cloud Climatology, https://doi.org/10.1175/JCLI-D-11-00666.1.

Foster, M. J., C. Phillips, A. K. Heidinger, E.E. Borbas, Y. Li, W.P. Menzel, A. Walther, and E. Weisz, 2023: PATMOS-x Version 6.0: 40 Years of Merged AVHRR and HIRS Global Cloud Data. *Journal of Climate*, **36**, 1143–1160, https://doi.org/10.1175/JCLI-D-22-0147.1.

George, R.C., and R. Wood, 2010: Subseasonal variability of low cloud radiative properties over the southeast Pacific Ocean. *Atmospheric Chemistry and Physics*, **10**, 4047–4063, https://doi.org/10.5194/acp-10-4047-2010.

Goessling, H.F., T. Rackow, and T. Jung, 2025: Recent global temperature surge intensified by record-low planetary albedo. *Science*, **387**, 68–73, https://doi.org/10.1126/science.adq7280.

Hang, Y., T.S. L'Ecuyer, D.S. Henderson, A.V. Matus, and Z. Wang, 2019: Reassessing the Effect of Cloud Type on Earth's Energy Balance in the Age of Active Spaceborne Observations. Part II: Atmospheric Heating, https://doi.org/10.1175/JCLI-D-18-0754.1.

He, T., S. Liang, and D. Song, 2014: Analysis of global land surface albedo climatology and spatial-temporal variation during 1981–2010 from multiple satellite products. *JGR Atmospheres*, **119**, https://doi.org/10.1002/2014JD021667.

Heidinger, A.K., C. Cao, and J.T. Sullivan, 2002: Using Moderate Resolution Imaging Spectrometer (MODIS) to calibrate advanced very high resolution radiometer reflectance channels. *Journal of Geophysical Research: Atmospheres*, **107**, AAC 11-1-AAC 11-10, https://doi.org/10.1029/2001JD002035.

Heidinger, A.K., J.T. Sullivan, and C.R.N. Rao, 2003: Calibration of visible and near-infrared channels of the NOAA-12 AVHRR using time series of observations over deserts. *International Journal of Remote Sensing*, **24**, 3635–3649, https://doi.org/10.1080/0143116021000023907.

Heidinger, A.K., W.C. Straka III, C.C. Molling, J.T. Sullivan, and X. Wu, 2010: Deriving an inter-sensor consistent calibration for the AVHRR solar reflectance data record. *International Journal of Remote Sensing*, **31**, 6493–6517, https://doi.org/10.1080/01431161.2010.496472.

Heidinger, A.K., M.J. Foster, A. Walther, and X. Zhao, 2014: The Pathfinder Atmospheres–Extended AVHRR Climate Dataset, https://doi.org/10.1175/BAMS-D-12-00246.1.

Kaufman, Y.J., and B.N. Holben, 1993: Calibration of the AVHRR visible and near-IR bands by atmospheric scattering, ocean glint and desert reflection. *International Journal of Remote Sensing*, **14**, 21–52, https://doi.org/10.1080/01431169308904320.

Klein, S.A., Y. Zhang, M.D. Zelinka, R. Pincus, J. Boyle, and P.J. Gleckler, 2013: Are climate model simulations of clouds improving? An evaluation using the ISCCP simulator. *Journal of Geophysical Research: Atmospheres*, **118**, 1329–1342, https://doi.org/10.1002/jgrd.50141.

Lattanzio, A., and Coauthors, 2013: Land Surface Albedo from Geostationary Satellites: A Multiagency Collaboration within SCOPE-CM, https://doi.org/10.1175/BAMS-D-11-00230.1.

L'Ecuyer, T.S., Y. Hang, A.V. Matus, and Z. Wang, 2019: Reassessing the Effect of Cloud Type on Earth's Energy Balance in the Age of Active Spaceborne Observations. Part I: Top of Atmosphere and Surface, https://doi.org/10.1175/JCLI-D-18-0753.1.

Liu, Y., W. Wu, M.P. Jensen, and T. Toto, 2011: Relationship between cloud radiative forcing, cloud fraction and cloud albedo, and new surface-based approach for determining cloud albedo. *Atmospheric Chemistry and Physics*, **11**, 7155–7170, https://doi.org/10.5194/acp-11-7155-2011.

Loeb, N.G., 1997: In-flight calibration of NOAA AVHRR visible and near-IR bands over Greenland and Antarctica. *International Journal of Remote Sensing*, **18**, 477–490, https://doi.org/10.1080/014311697218908.

Lopez, P., 2007: Cloud and Precipitation Parameterizations in Modeling and Variational Data Assimilation: A Review, https://doi.org/10.1175/2006JAS2030.1.

Lorente, A., K.F. Boersma, P. Stammes, L.G. Tilstra, A. Richter, H. Yu, S. Kharbouche, and J.P. Muller, 2018: The importance of surface reflectance anisotropy for cloud and NO_2

retrievals from GOME-2 and OMI. *Atmospheric Measurement Techniques*, **11**, 4509–4529, https://doi.org/10.5194/amt-11-4509-2018.

Matus, A.V., and T.S. L'Ecuyer, 2017: The role of cloud phase in Earth's radiation budget. *Journal of Geophysical Research: Atmospheres*, **122**, 2559–2578, https://doi.org/10.1002/2016JD025951.

Mueller, R., J. Trentmann, C. Träger-Chatterjee, R. Posselt, and R. Stöckli, 2011: The Role of the Effective Cloud Albedo for Climate Monitoring and Analysis. *Remote Sensing*, **3**, 2305–2320, https://doi.org/10.3390/rs3112305.

Nagaraja Rao, C.R., and J. Chen, 1996: Post-launch calibration of the visible and near-infrared channels of the Advanced Very High Resolution Radiometer on the NOAA-14 spacecraft. *International Journal of Remote Sensing*, **17**, 2743–2747, https://doi.org/10.1080/01431169608949104.

Nagol, J.R., E.F. Vermote, and S.D. Prince, 2014: Quantification of Impact of Orbital Drift on Inter-Annual Trends in AVHRR NDVI Data. *Remote Sensing*, **6**, 6680–6687, https://doi.org/10.3390/rs6076680.

Norris, J.R., and A.T. Evan, 2015: Empirical Removal of Artifacts from the ISCCP and PATMOS-x Satellite Cloud Records, https://doi.org/10.1175/JTECH-D-14-00058.1.

Perovich, D.K., 2018: Sunlight, clouds, sea ice, albedo, and the radiative budget: the umbrella versus the blanket. *The Cryosphere*, **12**, 2159–2165, https://doi.org/10.5194/tc-12-2159-2018.

Qu, X., A. Hall, S.A. Klein, and P.M. Caldwell, 2014: On the spread of changes in marine low cloud cover in climate model simulations of the 21st century. *Clim Dyn*, **42**, 2603–2626, https://doi.org/10.1007/s00382-013-1945-z.

Ramanathan, V., R.D. Cess, E.F. Harrison, P. Minnis, B.R. Barkstrom, E. Ahmad, and D. Hartmann, 1989: Cloud-Radiative Forcing and Climate: Results from the Earth Radiation Budget Experiment. *Science*, **243**, 57–63, https://doi.org/10.1126/science.243.4887.57.

Rossow, W.B., and R.A. Schiffer, 1999: Advances in Understanding Clouds from ISCCP. *Bull. Amer. Meteor. Soc.*, **80**, 2261–2287, https://doi.org/10.1175/1520-0477(1999)080%253C2261:AIUCFI%253E2.0.CO;2.

Sohn, B.J., S.H. Ham, and P. Yang, 2009: Possibility of the Visible-Channel Calibration Using Deep Convective Clouds Overshooting the TTL, https://doi.org/10.1175/2009JAMC2197.1.

Taylor, K. E., M. Crucifix, P. Braconnot, C.D. Hewitt, C. Doutriaux, A.J. Broccoli, J.F.B. Mitchell, and M.J. Webb, 2007: Estimating Shortwave Radiative Forcing and Response in Climate Models, https://doi.org/10.1175/JCLI4143.1.

Trenberth, K.E., J.T. Fasullo, and J. Kiehl, 2009: Earth's Global Energy Budget, https://doi.org/10.1175/2008BAMS2634.1.

Vermote, E.F., and N.Z. Saleous, 2006: Calibration of NOAA16 AVHRR over a desert site using MODIS data. *Remote Sensing of Environment*, **105**, 214–220, https://doi.org/10.1016/j.rse.2006.06.015.

Xiong, X. and Coauthors, 2018: Updates of Moderate Resolution Imaging Spectroradiometer on-orbit calibration uncertainty assessments. *JARS*, **12**, 034001, https://doi.org/10.1117/1.JRS.12.034001.

Zhan, C., and S. Liang, 2022: Improved estimation of the global top-of-atmosphere albedo from AVHRR data. *Remote Sensing of Environment*, **269**, 112836, https://doi.org/10.1016/j.rse.2021.112836.

Zhang, J., and G. Feingold, 2023: Distinct regional meteorological influences on low-cloud albedo susceptibility over global marine stratocumulus regions. *Atmospheric Chemistry and Physics*, **23**, 1073–1090, https://doi.org/10.5194/acp-23-1073-2023.